

Grasping and Control of Multi-Fingered Hands

Luigi Villani, Fanny Ficuciello, Vincenzo Lippiello, Gianluca Palli,
Fabio Ruggiero, Bruno Siciliano

Abstract An important issue in controlling a multi-fingered robotic hand grasping an object is the evaluation of the minimal contact forces able to guarantee the stability of the grasp and its feasibility. This problem can be solved online if suitable sensing information is available. In detail, using finger tactile information and contact force measurements, an efficient algorithm is developed to compute the optimal contact forces, assuming that, during the execution of a manipulation task, both the position of the contact points on the object and the wrench to be balanced by the contact forces may change with time. Since manipulation systems can be redundant also if the single fingers are not –due to the presence of the additional degrees of freedom (DOFs) provided by the contact variables– suitable control strategies taking advantage of such redundancy are adopted, both for single and dual-hand manipulation tasks. Another goal pursued in DEXMART is the development of a human-like grasping approach inspired to neuroscience studies. In order to simplify the synthesis of a grasp, a configuration subspace based on few predominant postural synergies of the robotic hand is computed. This approach is evaluated at kinematic level, showing that power and precise grasps can be performed using up to the third predominant synergy.

L. Villani, F. Ficuciello, V. Lippiello, F. Ruggiero, B. Siciliano
PRISMA Lab, Dipartimento di Informatica e Sistemistica,
Università degli Studi di Napoli Federico II, via Claudio 21, 80125 Napoli, Italy
email: {luigi.villani,fanny.ficuciello,vincenzo.lippiello,fabio.ruggiero,bruno.siciliano}@unina.it

G. Palli
Dipartimento di Elettronica Informatica e Sistemistica,
Alma Mater Studiorum Università di Bologna, viale Risorgimento 2, 40136 Bologna, Italy
email: gianluca.palli@unibo.it

1 Grasping Force Optimization

The control of a robotic system equipped with multi-fingered hands involves several aspects which range from the synthesis of the optimal grasping contact points and grasp planning, to the load sharing and grasp control. With respect to this last, the evaluation of the grasping forces able to guarantee the stability of the grasp and its feasibility, in the face of the external disturbances, represents a crucial problem. The complexity of the problem relies on the necessity of resolving online an optimization problem where both constraints and objective functions are nonlinear, the number of variable and constraints are relatively large, and the grasp configuration and the load wrench may change with time.

The force closure [41] and the optimal grasp configuration selection problems are not considered here, as they would be in charge of the grasp planner. On the other hand, the grasping force optimization problem has been intensively investigated only for relative simple robotic systems and not yet explicitly in the case of bimanual human-like robotic systems. For this last, the computational complexity becomes a major issue to be considered for an efficient online solution.

The nonlinearity of the contact friction models (point contact with friction or soft-finger contact) complicates the solution of the optimal contact force distribution problem. In [26] the friction cone constraints have been formulated in terms of linear matrix inequalities (LMIs), and the grasping optimization problem is addressed as a convex optimization problem involving LMIs with the $\max\text{-det}$ function as objective function. This problem can be efficiently solved with the interior point algorithm for a small number of fingers.

Starting from the observation that verifying the friction cone constraints is equivalent to testing the positive definiteness of certain symmetric matrices, in [11] the grasp force optimization has been formulated as a convex optimization problem on a Riemannian manifold with linear constraints. Several gradient flow type algorithms have been proposed to provide solutions suitable for real-time applications [12]; to reduce complexity of matrix inversion, the computation of the solution can be split into an on-line phase and an off-line phase, and sparse matrix techniques can be adopted [30]. This technique has been employed and experientially tested with an impedance control approach addressing the regrasping problem for dextrous manipulation tasks [54].

A further improvement has been presented in [27], consisting in a new compact semidefinite representation of the friction cone constraints which allows a significant reduction of the dimension of the optimization problem. Moreover, an estimation technique and a recursion method for selecting the step size in the gradient algorithm are proposed, together with the proof of the quadratic convergence of the algorithm.

In [50] and [53] a method based on the minimization of a cost function, which gives an analytical solution but does not ensure by itself the satisfaction of the friction constraints is presented. An iterative correction algorithm allows modifying this function until the internal forces enter the friction cone, resulting in a fast sub-optimal solution suitable for real-time applications. The grasping force optimization

problem in the case of power grasp is addressed in [60]. In this case, the optimization problem is formulated as a convex optimization problem involving LMIs similarly to [26], but considering a decomposition of the contact force space into four orthogonal subspaces of active and passive forces.

The method proposed in [11] requires the on-line pseudo-inversion of a constrained matrix whose dimension linearly increases with the number of fingers with a factor that depends on the contact type. By adopting the frictional cone constraint matrix representation proposed in [27], the dimension of the problem decreases and the solution can be computed in real time. However, if torque limits constraints are considered, the complexity of the problem increases more than quadratically with the number of joints, which is higher in a dual-hand system, making it unsuitable for real-time applications. Moreover, all the proposed solutions require, at each iteration, the evaluation of an initial point that satisfies the frictional cone constraints and the joint torque limits. The initial point can be computed with the method proposed in [34], but at the expense of a significant computational effort.

The proposed algorithm is based on the compact formulation of [27] and on the solution of a convex optimization case as in [12], and it extends to bimanual manipulation systems our previous works on single-hand manipulation [32], [33]. The method allows considering also joint torque constraints, with a minimum increase of computation complexity, compatible with real-time constraints. Moreover, the iterative formulation does not require the evaluation at each step of a new initial point. Finally, a sub-optimal single-hand optimization algorithm is proposed to cope with very limited computational hardware availability, and compared with the optimal solution. In particular, a new criterion for load sharing [61], [58], [56] between the hands is here introduced to improve the solution. The feasibility and the effectiveness of this approach have been tested in a simulation scenario where a robotic torso equipped with two dextrous hands is used to empty a half-filled bottle.

1.1 Problem Formulation

Consider a bimanual robotic system equipped with two multi-fingered hands grasping an object with n contacts between the object and the fingertips, the links of the fingers and the palm. Denote the contact wrench of the grasp with $\mathbf{c} = [\mathbf{c}_r^T \ \mathbf{c}_l^T]^T = [\mathbf{c}_1^T \ \dots \ \mathbf{c}_n^T]^T \in \mathbb{R}^{2m}$, where $\mathbf{c}_i \in \mathbb{R}^m$ is the wrench vector of the i -th contact with dimension m depending from the adopted contact model, and \mathbf{c}_r and \mathbf{c}_l are the corresponding wrench vectors of all the contact points of the right and left hand, respectively.

The grasping force optimization problem (GFO) consists in finding the set of contact wrenches balancing the generalized external force $\mathbf{h}_e \in \mathbb{R}^6$ acting on the object (including object inertia and weight), which are feasible with respect to the kinematic structure of the hand and to the corresponding joint torque limits, and minimize the overall stress applied the object, i.e., the internal forces. Moreover, to

avoid the slippage of the fingers on the object surface, each contact wrench has to be confined within the friction cone.

The balance equation for the generalized forces applied to the object can be written in the form

$$\mathbf{h}_e = \mathbf{G}\mathbf{c}, \quad (1)$$

where $\mathbf{G} = [\mathbf{G}_r \ \mathbf{G}_l] \in \mathbb{R}^{6 \times nm}$ is the grasp map composed of the the grasp matrices of the right and left hand, which is full rank for force-closure grasps [41]. It is assumed that the contact point configurations ensuring the force-closure constraint are assigned at each time by the planning system.

Although several contact models can be used, the two usually adopted are the *point contact with friction* (PCWF) model and the *soft finger contact* (SFC) model.

In the PCWF case, the contact wrench has three DOFs ($m = 3$): the normal component $c_{i,z}$ to the object surface and the two components $c_{i,x}$, $c_{i,y}$ on the tangent plane. The friction constraint is represented by the law

$$\frac{1}{\mu_i^2} (c_{i,x}^2 + c_{i,y}^2) \leq c_{i,z}^2 \text{ and } c_{i,z} > 0, \quad (2)$$

where μ_i is the friction coefficient at the i -th contact point.

In the SFC case, the contact wrench has an additional DOF $c_{i,t}$ ($m = 4$), corresponding to the torsional component of the moment about the contact normal. In this case, the friction constraint in an elliptic approximation can be expressed in the form

$$\frac{1}{\mu_i} (c_{i,x}^2 + c_{i,y}^2) + \frac{1}{\mu_{i,t}} c_{i,t}^2 \leq c_{i,z}^2 \text{ and } c_{i,z} > 0, \quad (3)$$

where μ_i and $\mu_{i,t}$ denote the tangential and torsion friction coefficients at the i -th contact point, respectively.

The balance equation for the torques applied to fingers joints of the hand can be written in the form

$$\mathbf{J}^T(\mathbf{q})\mathbf{c} + \boldsymbol{\tau}_e = \boldsymbol{\tau}, \quad (4)$$

where and $\mathbf{J}(\mathbf{q}) = [\mathbf{J}_r^T \ \mathbf{J}_l^T]^T$ is the $(nm \times l)$ hands Jacobian matrix, depending on the $(l$ -dimensional) vector \mathbf{q} of the joint variables, being l the total number of the joints, $\boldsymbol{\tau}_e$ is the external torque, including gravity, Coriolis, centripetal and inertia effects at the fingers joints, and $\boldsymbol{\tau}$ is the torque provided by the actuators. For simplicity, it is assumed that $\mathcal{N}(\mathbf{J}^T) = \emptyset$, meaning the absence of structurally dependent forces, namely, contact forces not caused by joint torques but depending on hand mechanics (see, e.g., [41]).

To ensure that the joint actuators are able to provide the required torques, a joint torque constraint must also be considered

$$\boldsymbol{\tau}_L \leq \boldsymbol{\tau} \leq \boldsymbol{\tau}_U, \quad (5)$$

where $\boldsymbol{\tau}_L$ ($\boldsymbol{\tau}_U$) is the lower (upper) joint torque limit.

The simultaneous satisfaction of the force balance equation (1), with the friction constraints (2) and (3), and of the joint torque balance equation (4) with constraint (5), implies that the grasp is stable and feasible. The GFO problem considered here consists in finding the optimal grasp wrench that minimizes the internal forces acting on the object, under the above constraints. The internal forces are contact wrenches that satisfy the friction cone constraints and belong to the null space of the grasp matrix \mathbf{G} . These wrenches \mathbf{c}_{int} do not contribute to the balance equation (1), being $\mathbf{G}\mathbf{c}_{int} = 0$, but are used to satisfy the friction cone constraints at the contact points.

1.2 Grasping Constraints and Cost Function

The frictional inequalities (2) and (3) are equivalent to the positive definiteness of the block-diagonal matrix [27]

$$\mathbf{F}(\mathbf{c}) = \text{diag}(\mathbf{F}_1(\mathbf{c}_1), \dots, \mathbf{F}_n(\mathbf{c}_n)) > 0, \quad (6)$$

where $\mathbf{F}_i(\mathbf{c}_i)$ is the symmetric (2×2) matrix

$$\mathbf{F}_i(\mathbf{c}_i) = \begin{bmatrix} c_{i,z} + \frac{c_{i,x}}{\mu_i} & \frac{c_{i,y}}{\mu_i} \\ \frac{c_{i,y}}{\mu_i} & c_{i,z} - \frac{c_{i,x}}{\mu_i} \end{bmatrix} \quad (7)$$

in the PCWF case, while it is the Hermitian (2×2) matrix

$$\mathbf{F}_i(\mathbf{c}_i) = \begin{bmatrix} c_{i,z} + \frac{c_{i,x}}{\sqrt{\mu_i}} & \frac{c_{i,y}}{\sqrt{\mu_i}} - j \frac{c_{i,t}}{\sqrt{\mu_{i,t}}} \\ \frac{c_{i,y}}{\sqrt{\mu_i}} + j \frac{c_{i,t}}{\sqrt{\mu_{i,t}}} & c_{i,z} - \frac{c_{i,x}}{\sqrt{\mu_i}} \end{bmatrix}, \quad (8)$$

in the SFC case.

Similarly, the torque limit constraint (5), in view of the torque balance equation (4), is equivalent to the positive definiteness of the diagonal matrix

$$\mathbf{T}(\mathbf{c}, \mathbf{q}, \tau_e) = \text{diag}(\tau_B) > 0, \quad (9)$$

where

$$\tau_B = \begin{bmatrix} \tau_{B,L} \\ \tau_{B,H} \end{bmatrix} = \begin{bmatrix} \mathbf{J}^T(\mathbf{q})\mathbf{c} - \tau_L + \tau_e \\ -\mathbf{J}^T(\mathbf{q})\mathbf{c} + \tau_H - \tau_e \end{bmatrix} \quad (10)$$

contains the distances of actuator torques from the lower ($\tau_{B,L}$) and upper ($\tau_{B,H}$) limits, respectively.

Hence, the simultaneous satisfaction of both frictional and joint torque constraints is equivalent to the positive definiteness of the linearly constrained block-diagonal matrix

$$\mathbf{P} = \text{diag}(\mathbf{F}, \mathbf{T}) > 0. \quad (11)$$

Notice that the elements of the matrices \mathbf{F} and \mathbf{T} are linearly dependent, because both depend on \mathbf{c} . Moreover, the force balance equation (1) and the torque balance equation (4) corresponds to linear constraints imposed on matrix \mathbf{P} .

By denoting with $\mathbf{c}(\mathbf{F})$ the contact wrench vector extracted from the frictional constraint matrix, with $\boldsymbol{\tau}_B(\mathbf{T})$ the vector composed by the diagonal elements of \mathbf{T} , and defining vector $\boldsymbol{\xi}(\mathbf{P}) = [\mathbf{c}(\mathbf{F})^T \boldsymbol{\tau}_B(\mathbf{T})^T]^T$, the linear constraints on matrix \mathbf{P} imposed by (1) and (4) can be represented in the following affine general form

$$\mathbf{A}\boldsymbol{\xi}(\mathbf{P}) = \mathbf{b} \quad (12)$$

with

$$\mathbf{A} = \begin{bmatrix} \mathbf{G} & \mathbf{0}_{6 \times 2l} \\ \mathbf{A}_\tau & \end{bmatrix} \quad \mathbf{b} = \begin{bmatrix} \mathbf{h}_e \\ \tau_L - \tau_e \\ \tau_H - \tau_e \end{bmatrix}, \quad (13)$$

where \mathbf{A}_τ is a $(2l \times nm + 2l)$ matrix defined as follows

$$\mathbf{A}_\tau = \begin{bmatrix} \mathbf{J}(\mathbf{q})^T & -\mathbf{I}_l & \mathbf{0}_l \\ \mathbf{J}(\mathbf{q})^T & \mathbf{0}_l & \mathbf{I}_l \end{bmatrix}, \quad (14)$$

being $\mathbf{0}_\times$ the null matrix and \mathbf{I}_\times the identity matrix of the indicated dimensions.

The optimization procedure is based on the minimization of the cost function $\Phi(\mathbf{P}) : \mathcal{P}(r) \rightarrow \mathbb{R}$, being $\mathcal{P}(r)$ the set of positive definite symmetric $(r \times r)$ matrices $\mathbf{P} = \mathbf{P}^T > 0$, defined as

$$\Phi(\mathbf{P}) = \text{tr}(\mathbf{W}_p \mathbf{P} + \mathbf{W}_b \mathbf{P}^{-1}), \quad (15)$$

where $\text{tr}(\cdot)$ denotes the trace operator, \mathbf{W}_p and \mathbf{W}_b are positive definite symmetric matrices. Notice that Φ is a strictly convex twice continuously differentiable function on $\mathcal{P}(r)$ and $\Phi(\mathbf{P}) \rightarrow +\infty$ for $\mathbf{P} \rightarrow \partial \mathcal{P}(r)$, being $\partial \mathcal{P}(r)$ the boundary of $\mathcal{P}(r)$.

By noting that the sum of the elements of \mathbf{T} (i.e. of $\boldsymbol{\tau}_B$) is constant for each \mathbf{c} , because the sum of the two joint torque constraints for the i -th joint is constant and equal to $\tau_{H,i} - \tau_{L,i}$, the diagonal weighting matrix $\mathbf{W}_p = \text{diag}(w_p \mathbf{I}_6, \mathbf{0}_{2l})$, with $w_p > 0$, is considered. In this way, the term $\mathbf{W}_p \mathbf{P}$ weights only the normal forces $\mathbf{c}_{i,z}$ at each contact point, i.e. the pressure forces on the object. If required, different weights can be used allowing higher contact forces for strongest fingers.

The second term $\mathbf{W}_b \mathbf{P}^{-1}$ represents a barrier function, which goes to infinity when \mathbf{P} tends to a singularity, i.e. when friction or torque limits are approached. The barrier weight matrix is also chosen diagonal $\mathbf{W}_b = \text{diag}(\mathbf{W}_{b,F}, \mathbf{W}_{b,T})$, with

$$\begin{aligned} \mathbf{W}_{b,F} &= w_{b,F} \text{diag}(\mu_1, \dots, \mu_n) \\ \mathbf{W}_{b,T} &= w_{b,T} \text{diag}(\tau_{H,1} - \tau_{L,1}, \dots, \tau_{H,l} - \tau_{L,l}, \\ &\quad \tau_{H,1} - \tau_{L,1}, \dots, \tau_{H,l} - \tau_{L,l}), \end{aligned} \quad (16)$$

being $w_{b,F} > 0$ and $w_{b,T} > 0$.

Hence, the minimization of the cost function (15) with the linear constraint (12) corresponds to the minimization of the normal contact wrench components applied to the object while satisfying the friction and torque constraints.

1.3 Semidefinite Programming

The minimization problem can be solved using the linearly constrained gradient flow approach on the smooth manifold of positive definite matrices presented in [28], [11]. In particular, it is possible to prove that $\Phi(\mathbf{P})$ presents a unique minimum that can be reached through the linear constrained exponentially convergent gradient flow

$$\dot{\xi}(\dot{\mathbf{P}}) = \mathbf{Q}\xi(\mathbf{P}^{-1}\mathbf{W}_b\mathbf{P}^{-1} - \mathbf{W}_p), \quad (17)$$

where $\mathbf{Q} = (\mathbf{I} - \mathbf{A}^\dagger\mathbf{A})$ is the linear projection operator onto the tangent space of \mathbf{A} , and $\mathbf{A}^\dagger = \mathbf{A}^T(\mathbf{A}\mathbf{A}^T)^{-1}$ is the pseudo-inverse of \mathbf{A} . Consequently, $\mathbf{A}\mathbf{Q} = \mathbf{0}$ and $\mathbf{A}\dot{\xi}(\dot{\mathbf{P}}) = \mathbf{0}$; hence, if the solution satisfies the constraint (12) at $t = 0$, it will satisfy the constraint for all $t > 0$.

A discrete-time version of (17) based on the Euler numerical integration algorithm is

$$\xi(\mathbf{P}_{k+1}) = \xi(\mathbf{P}_k) + \alpha_k \mathbf{Q}\xi(\mathbf{P}_k^{-1}\mathbf{W}_b\mathbf{P}_k^{-1} - \mathbf{W}_p), \quad (18)$$

where the step size α_k is chosen to ensure down hill steps. Notice that the choice of α_k strongly affects the performance of the optimization algorithm. A wrong choice could determine a very slow convergence or the break of the barrier. Several strategies have been proposed for the self-tuning of α_k at each iteration (see [34] for details). The sensitivity to the step size choice can be reduced by adopting a Dikin-type recursive algorithm [12], [19], that leads to the discrete flow

$$\xi(\mathbf{P}_{k+1}) = \xi(\mathbf{P}_k) - \alpha_k \mathbf{Q} \frac{\xi(\mathbf{P}_k^{-1}\mathbf{W}_b\mathbf{P}_k^{-1} - \mathbf{W}_p)}{\|\mathbf{P}_k^{-1}\mathbf{W}_b\mathbf{P}_k^{-1} - \mathbf{W}_p\|_{P_k}}, \quad (19)$$

where $\|\mathbf{X}\|_Y = \text{tr}(\mathbf{Y}^{-1}\mathbf{X}\mathbf{Y}^{-1}\mathbf{X})$, and $0 \leq \alpha_k \leq 1$ can be evaluated with a bounded line search minimizing $\Phi(\mathbf{P}_{k+1})$.

The online implementation of the proposed algorithm requires the inversion of a $(6 + 2l)$ square matrix $\mathbf{A}\mathbf{A}^T$ needed for the evaluation of \mathbf{A}^\dagger at each iteration, also when the grasping configuration is unchanged, i.e. when \mathbf{G} is constant, due to the variation of $\mathbf{J}(\mathbf{q})$.

Starting from the discrete version of the gradient flow (18), the following new formulation can be derived

$$\mathbf{c}_{k+1} = \mathbf{c}_k + \alpha_k \bar{\mathbf{Q}}\xi(\mathbf{P}^{-1}(\mathbf{c}_k)\mathbf{W}_b\mathbf{P}^{-1}(\mathbf{c}_k) - \mathbf{W}_p), \quad (20)$$

where $\bar{\mathbf{Q}} = (\mathbf{I} - \mathbf{G}^\dagger\mathbf{G})[\mathbf{I}_{nm}\mathbf{0}_{2l}](\mathbf{I} - \mathbf{A}_\tau^\dagger\mathbf{A}_\tau)$ is the result of the projection onto the null space of matrix \mathbf{A}_τ in (14), which guarantees the coherence of the elements of matrix

\mathbf{P} , and of the subsequent projection onto the null space of the grasp matrix, ensuring the force balance constraint (1). Therefore, the evaluation of the inverse of a $6 + 2l$ square matrix is decomposed into the evaluation of the inverse of two matrices of lower dimensions (6 and $2l$, respectively). Moreover, if the grasp configuration remains unchanged, the projector depending on \mathbf{G} can be evaluated off-line. A similar decomposition can be easily achieved for the gradient flow (19).

1.4 Improvements for Real-Time Applications

An iterative technique for the on-line evaluation, at each sampling time, of the initial point—the initial solution \mathbf{P}_0 for the optimization gradient flow algorithm—is proposed here, based on the optimal solution at the previous sampling time. The quantities that can vary between successive sampling times are the hand configuration \mathbf{q} , the external torque τ_e , and the grasp map \mathbf{G} , while they are taken constant during the iterations of the optimization algorithm between two consecutive sampling times (optimization cycle).

To avoid the evaluation of an initial point at each sampling time, the following approach is proposed. Initially, at time t_0 , the method proposed in [34] (or an equivalent one) is used to evaluate off-line a first valid initial solution, which is employed for the first optimization cycle. For the next sampling times t_k , the initial point is computed from the optimal solution \mathbf{c}_{k-1} computed at the end of the previous optimization cycle, through the iterative algorithm

$$\begin{aligned}\bar{\mathbf{c}}_j &= (\mathbf{I} - \mathbf{G}_k^\dagger \mathbf{G}_k) \bar{\mathbf{c}}_{j-1} + \gamma_j \mathbf{G}_k^\dagger \mathbf{h}_{e,k} + (1 - \gamma_j) \mathbf{G}_{k-1}^\dagger \mathbf{h}_{e,k-1} \\ \bar{\boldsymbol{\tau}}_j &= \mathbf{J}^T (\gamma_j \mathbf{q}_k + (1 - \gamma_j) \mathbf{q}_{k-1}) \bar{\mathbf{c}}_j + \gamma_j \boldsymbol{\tau}_{e,k} + (1 - \gamma_j) \boldsymbol{\tau}_{e,k-1},\end{aligned}\quad (21)$$

with initial condition $\bar{\mathbf{c}}_0 = \mathbf{c}_{k-1}$, where the subscript k is referred to the current optimization cycle, while the subscript j and the variables with the bar are referred to the iterations within the cycle. The coefficient $\gamma_j \in (0, 1]$ is chosen at each iteration according to a monotone sequence, using a simple linear search algorithm, as the maximum value that does not produce invalid solutions ($\mathbf{P}_0 \leq 0$). In the worst case, γ_0 must be set to a value close to zero.

In detail, at each step of the optimization cycle, the first equation of (21) gradually modifies the external wrench component of the current solution until the full external wrench $\mathbf{h}_{e,k}$ is balanced (i.e., $\gamma_j = 1$). Obviously, the optimization cycle cannot be terminated until γ_j does not reach 1. If the solution evaluated at the previous sampling time (\mathbf{c}_{k-1}) is sufficiently far from the boundaries (the distance depends also from the weights assigned to \mathbf{W}_b), γ_0 can be set to 1 at the first iteration, and thus the initial point has the same internal wrench component of the previous optimal solution. On the other hand, when $\gamma_0 < 1$, the effect of the barrier function produces a new solution that, at each iteration of the optimization cycle, goes away from the boundaries; this guarantees that γ_j increases at each step, until $\gamma_j = 1$. The second equation is required to modify the joint torque with the same rationale of

the first equation. In sum, the sequence γ_j produces an effect similar to a low-pass filter on the variation of the solutions between subsequent optimization steps that are recovered directly within the recursive optimization algorithm.

From the practical experience, if the weight \mathbf{W}_b of the barrier function in the cost function (15) is chosen high enough and the sampling period is small, in most cases the last optimal solution is a valid initial solution, i.e. $\gamma_0 = 1$.

Under the reasonable assumption that the solutions of the optimization algorithm evaluated at successive sampling times are quite close, the joint torque constraints can be simplified observing that not all the joint torque constraints can be effective simultaneously. For example, if, for the current optimal solution, the actuator of joint i provides a torque close to the upper bound $\tau_{H,i}$, the constraint on the lower bound $\tau_{L,i}$ can be deactivated at the next sampling time, being negligible the corresponding barrier term in the cost function. More in general, if for a grasp configuration a given contact force is required along a certain direction, it is reasonable to assume that the corresponding joint torques will not change significantly at the next sampling time. Starting from this observation, the number of joint torque constraints can be dynamically reduced at each sampling time, by using the distance of the torque evaluated at the previous sampling time from the lower and upper bounds as the criterion for selecting the constraint (the lower or the upper one) that needs to be activated. Only those constraints with a distance higher than a torque limit threshold, that can be chosen as a fraction $\sigma_\tau > 0$ of the corresponding torque limit, will be activated.

Wherever required, to reduce chattering phenomena during the activation and deactivation of a constraint, that can introduce noise in the solution, a simple double threshold ($\sigma_{\tau,L} > 0$ and $\sigma_{\tau,H} > 0$) with a hysteretic threshold can be employed.

For applications with limited computational resource, a further simplification in the algorithm can be introduced by splitting the bimanual optimization problem into two simpler single-hand problems. In this case, the initial point iterative self-evaluation algorithm presented above can be employed to find the initial common solution. Then two independent optimization procedures can be started separately for each hand, and the corresponding solutions are composed only at the end to achieve a unique wrench vector solution. The price to pay with the simplified algorithm is that the solution is not optimal in a global sense.

A significant improvement in the solution can be reached by considering a suitable weighted pseudo-inverse of the grasp matrix in (21), with the goal of achieving a load sharing between the hands in reason of the actual load of the hand actuators. In detail, at each sampling time, the minimum distance of the joint torques with respect to the corresponding limits is evaluated for each hand, namely $\delta_{\tau,r}$ and $\delta_{\tau,l}$ for the right and for the left hand, respectively. Then a weighting matrix

$$\mathbf{W}_G = \text{diag} \left(\frac{\delta_{\tau,r} + \delta_{\tau,l}}{\delta_{\tau,r}} \mathbf{I}_{n_r}, \frac{\delta_{\tau,r} + \delta_{\tau,l}}{\delta_{\tau,l}} \mathbf{I}_{n_l} \right), \quad (22)$$

with n_r and n_l the number of contact points for the right and for the left hand, is adopted for the evaluation of the weighed pseudo-inverse of the grasp matrix

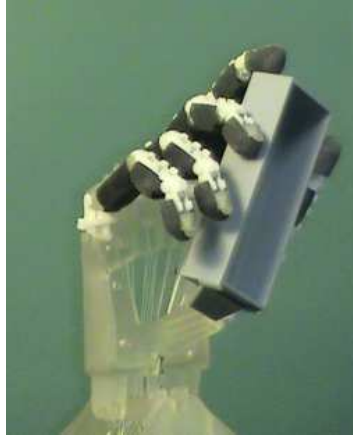


Fig. 1 The DEXMART Hand prototype.

$$\mathbf{G}^\# = \mathbf{W}_G^{-1} \mathbf{G} (\mathbf{G} \mathbf{W}_G^{-1} \mathbf{G}^T)^{-1}. \quad (23)$$

With this choice, the quadratic form $\mathbf{c}^T \mathbf{W}_G \mathbf{c}$ is minimized, reducing the load requirement on the hand closest to its torque limits. This approach, as demonstrated in the following case study, can produce a reduction up to 50% of the computational time when a large number of joint torque constraints are active.

1.5 Case Study

The proposed GFO algorithm has been tested in simulation using two models of the DEXMART Hand (see Fig.1), mounted on an anthropomorphic torso, as shown in Fig. 2. It is assumed that the hands grasp a cylinder representing a bottle half filled with water and the task consists in pouring water by reorienting the bottle. The bottle is initially grasped with the main axis aligned to the vertical direction; then the task can be decomposed into three steps:

- a rotation of 135 deg about the horizontal axis through the geometric center of the cylinder is commanded;
- the hand is stopped while some water is poured from the bottle (the mass and inertia of the bottle change accordingly);
- the opposite rotation is commanded to set the bottle back to the initial pose.

A dynamic simulation has been performed using Matlab/Simulink, where the variation of the position of the center of mass of the water and that of its weight have been considered. Figure 2 shows on the right a section of the bottle half filled with water. In the figure, the intensity of the gravity force is proportional to the black vertical arrow applied to the instantaneous center of mass (of length proportional to

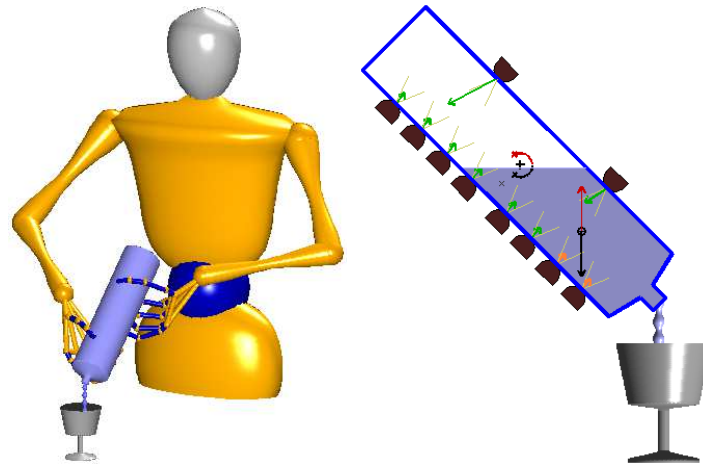


Fig. 2 *Left*: anthropomorphic torso with two DEXMART Hands grasping a bottle. *Right*: section of the grasped bottle with graphical representation of the gravity force and torque (black arrows), of the resultant force and torque applied by the fingers (red arrows), of the optimal contact forces (green arrows if not interested by joint torque constraints, orange arrow otherwise), and of the friction cones (yellow triangles).

the intensity of the force), while the intensity of the gravity torque with respect to the center of the bottle is proportional to the black gravity arrow. The red arrows represent the external force and torque balancing the gravity effects and resulting from the contact forces applied by the fingers, represented by green arrows if not interested by joint torque constraints, orange arrow otherwise. The sections of the friction cones in the contact points are colored in yellow. A sequence of significant configurations of the bottle during task execution is shown in Fig. 3.

The effectiveness of the friction and of joint torque limits constraints is shown by considering two different simulations: in the first one only the friction constraint is considered, without any constraint on the joint torque limits, while in the second one different torque limits are set for the fingers. In particular, the thumb actuators are considered stronger than the corresponding actuators of the other fingers of the hand (± 0.5 vs. ± 0.075 Nm), like for the human hand.

In Fig. 4 the trajectory and the areas covered by the contact force vector of each finger in the corresponding contact point during the bottle motion are shown, in blue (red) color for the case without (with) torque constraints. As expected, the frictional constraints are always respected in both simulation cases accordingly to the barrier function considered into the cost function (15).

The time history of the minimum distance of the joint torques for all the actuators from the corresponding limits is shown in Fig. 5, with the red (blue) line refers to the case with (without) torque constraints. The effect of the barrier function settled up also on torques insures the full respect of the adopted limits, without affecting significantly the contact wrenches as shown in Fig. 6.

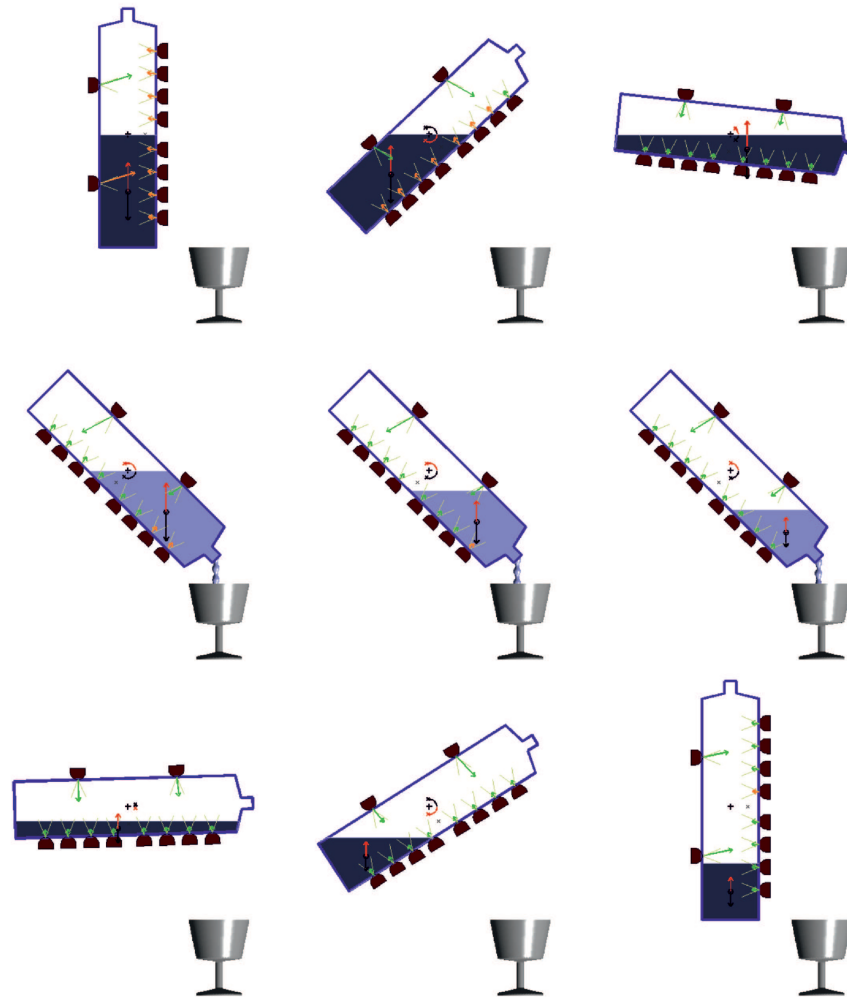


Fig. 3 Sequence of significant configurations of the bottle and of the forces during the task execution.

In Fig. 6 a comparison of the norm of the contact wrenches (on the left) and of the joint torques (on the right) is shown for both simulation cases. The differences for the norm of the torque between the two cases is very limited, while the contact wrenches are improved (smaller in norm), due to a better balancing of the load between the fingers.

The benefits resulting from the adoption of the online joint-torque constraints selection are shown in Fig. 7, where the time history of the computational time effort are represented on the left and the number of employed constraints are represented on the right. To remove the dependence on the employed hardware, all the

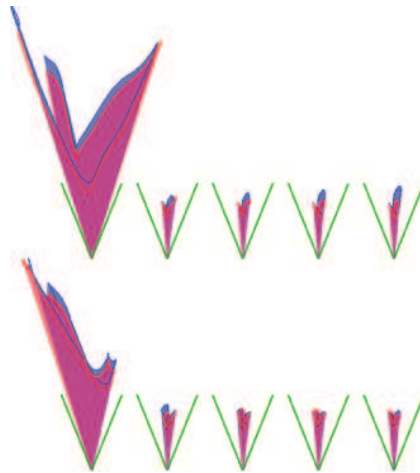


Fig. 4 Areas covered by the contact forces of each finger (*Top*: right hand, *Bottom*: left hand; from the left side: from the thumb to the little finger) without (blue color) and with (red color) torque constraints with respect to the friction cones (represented with green lines).

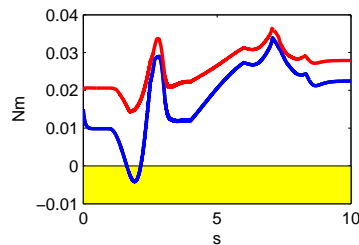


Fig. 5 Time history of the minimum distance of the joint torques from the corresponding limits for all the actuators, in red (blue) color for the case with (without) torque constraints. Negative values (the yellow area) correspond to the violation of one or more joint torque limits.

considered cases are normalized with respect to the maximum value of the fully constrained case (black line) to the value 100 (corresponding about to 23 ms on an Intel Pentium IV at 2.8 Ghz). In particular, four different cases are compared: all constraints (black lines), $\sigma_\tau = 0$ (red lines), $\sigma_\tau = 0.5$ (green lines), $\sigma_\tau = 0.8$ (blue lines), and unconstrained (gray lines), where σ_τ is the threshold for the activation of the joint torque constraints. The achieved reduction of the mean of the computational time varies from a minimum of about 30% for $\sigma_\tau = 0$ to a maximum of about 90% for $\sigma_\tau = 0.8$.

The adoption of the sub-optimal single-hand GFO algorithm can provide a significant reduction on the computational time with respect to the optimal one, as shown in Fig. 7 for the case of all joint torque constraint simultaneously active. However, the drawback is that the sub-optimal solution has reduced performance in terms of both the norm of contact wrenches and of joint torque (see Fig. 8). Consequently,

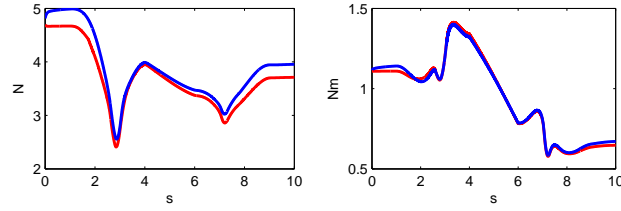


Fig. 6 Time history of the norm of the contact wrenches (on the left) and of the joint torques (on the right), in red (blue) color for the case with (without) torque constraints.

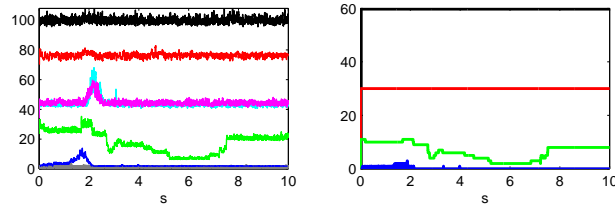


Fig. 7 Time history of the normalized computational-time effort (left) and of the number of employed joint torque constraints (right) for the cases with all constraints (black), $\sigma_\tau = 0$ (red), $\sigma_\tau = 0.5$ (green), $\sigma_\tau = 0.8$ (blue), unconstrained (gray), and single-hand local optimization with (violet) and without (cyan) weighted pseudo-inverse of the grasp matrix.

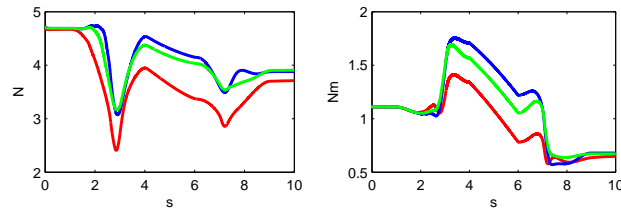


Fig. 8 Time history of the norm of the contact wrenches (on the left) and of the joint torques (on the right) for the cases of local single-hand optimization without (blue) and with (green) weighted pseudo-inverse of the grasp matrix, and global optimization (red).

also the distance with respect to the joint torque limits result reduced significantly, as shown in Fig. 9), but without violating the imposed constrained. As shown in these figures, the adoption of the weighted pseudo-inverse of the grasp matrix in (23) can improve the achieved solution resulting in a well-shared load between the two hands. This behavior is mainly due to the reduction of the DOFs available to the optimization algorithm considering separately the the two hands instead of both together.

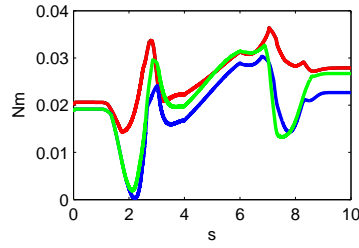


Fig. 9 Time history of the minimum distance of the joint torques from the corresponding limits for all the actuators for the cases of local single-hand optimization without (blue) and with (green) weighted pseudo-inverse of the grasp matrix, and global optimization (red).

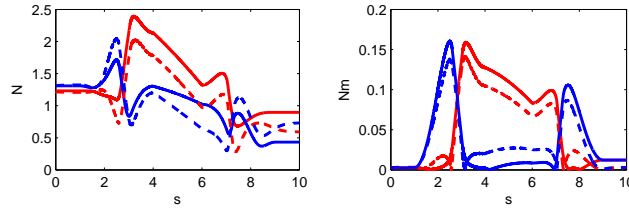


Fig. 10 Time history of the norm of the load force (on the *left*) and moments (on the *right*) for the right (red) and left (blue) hand in the cases of local (continuous lines) and global (dashed lines) method.

On top of Fig. 10 the time history of the normalized load-sharing coefficients $\delta_{\tau,r}/(\delta_{\tau,r} + \delta_{\tau,l})$ (red) and $\delta_{\tau,l}/(\delta_{\tau,r} + \delta_{\tau,l})$ (blue) employed in (23) is shown, while t

The time history of the norm of the load force and moments for the right (red) and left (blue) hand in the cases of sub-optimal (continuous lines) and optimal (dashed lines) method are shown in Fig. 10. As expected, the whole balancing of effort between the hands is degraded with respect to the optimal solution (dashed lines), but the adopted load sharing method allows an online load repartition according to the current load capability of each hand.

2 Kinematic Control With Force Feedback

Dual-arm/hand object manipulation with multi-fingered hands is a challenging task, especially in service robotics applications, but it has not investigated as extensively as it should deserve. In order to achieve the desired motion of the manipulated object, arms and fingers should operate in a coordinated fashion. In the absence of physical interaction between the fingers and the object, simple motion synchronization shall be ensured. Further, the execution of object grasping or manipulation requires controlling also the interaction forces to ensure grasp stability [43], [49].

From a kinematics point of view, an object manipulation task can be assigned in terms of the motion of the fingertips and/or in terms of the desired object motion. The planner (or the controller) has to map the desired task into the corresponding joint trajectories of the fingers and the arms, thus requiring the solution of an inverse kinematics problem.

In this work, starting from the framework presented in [31], a kinematic model for object manipulation using a dual-arm/hand robotic system is derived, which allows computing the object pose from the joint variables of each arm and each finger (active joints), as well as from a set of contact variables, modelled as passive joints [40]. Suitable conditions are derived ensuring that a given motion can be imposed to the object using only the active joints. Exploiting also the information provided by force sensors mounted inside the fingertips, a two-stage control scheme is proposed so as to achieve the desired object motion and to maintain the desired contact normal forces.

The kinematic redundancy of the system, deriving also from the presence of the passive joints, is suitably exploited to satisfy a certain number of secondary tasks with lower priority, aimed at ensuring grasp stability and manipulation dexterity—without violating system constraints—besides the main task corresponding to the desired object motion. To this aim, a prioritized task sequencing with smooth transitions between the different tasks [36] is employed.

At the best of authors knowledge, the focus of previous works on kinematics of multi-fingered manipulation was on constrained kinematic control [25], [40], or manipulability analysis [8], without considering redundancy resolution and the benefits of integrating a force feedback in a kinematic control loop. The effectiveness of the proposed approach is demonstrated in simulation by considering an object exchange task for a planar bimanual system.

2.1 Kinematic Model

Consider a bimanual manipulation system, e.g., the humanoid manipulator of Fig. 11 composed by a three DOFs torso and two DLR manipulators (each with seven DOFs). The direct kinematics can be computed as reported in [55], by introducing a frame Σ_b fixed with the base of the torso, two frames, Σ_r and Σ_l , attached at the base of the right and left arm, respectively, and two frames, Σ_{rh} and Σ_{lh} , attached to the palms of the right and left hand, respectively. Moreover, assuming that each arm ends with a robotic hand composed by N fingers, it is useful to introduce a frame Σ_{rf_i} (Σ_{lf_i}), attached to the distal phalanx of finger i ($i = 1 \dots N$) of the right (left) hand.

The pose of Σ_{rf_i} with respect to the base frame Σ_b can be represented by the well known (4×4) homogeneous transformation matrix $\mathbf{T}_{rf_i}^b(\mathbf{R}_{rf_i}^b, \mathbf{o}_{rf_i}^b)$, where $\mathbf{R}_{rf_i}^b$ is the (3×3) rotation matrix expressing the orientation of Σ_{rf_i} with respect to the base frame and $\mathbf{o}_{rf_i}^b$ is the (3×1) position vector of the origin of Σ_{rf_i} with respect to the base frame. Hence, the direct kinematics can be expressed as

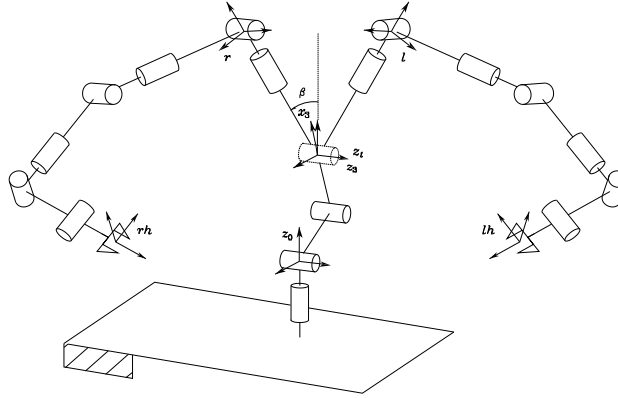


Fig. 11 Kinematic structure of a humanoid manipulator with torso and arms inspired to the DLR Justin.

$$\mathbf{T}_{rf_i}^b = \mathbf{T}_r^b(\mathbf{q}_t) \mathbf{T}_{rh}^r(\mathbf{q}_{rh}) \mathbf{T}_{rf_i}^{rh}(\mathbf{q}_{rf_i}) \quad (24)$$

where \mathbf{T}_r^b is the matrix relating the frame at the basis of the right arm to the base frame (which depends, in turn, on the torso joint vector, \mathbf{q}_t), $\mathbf{T}_{rh}^r(\mathbf{q}_{rh})$ is the matrix relating the right palm frame to the base frame of the right arm (which depends, in turn, on the joint vector of the right arm, \mathbf{q}_{rh}), and $\mathbf{T}_{rf_i}^{rh}$ is the matrix relating the frame attached to finger i to the palm frame of the right hand (which depends, in turn, on the joint vector \mathbf{q}_{rf_i} , where the fingers are assumed to be identical). An equation similar to (24) holds for the left hand fingers, with subscript l in place of subscript r .

Due to the branched structure of the manipulator, the kinematic equations of both the right and the left arm depend on the joint vector \mathbf{q}_t of the torso and, thus, they are not independent. Without loss of generality, hereafter it is assumed that the torso is motionless, i.e., \mathbf{q}_t is constant; therefore, the kinematics of the right and of the left hand can be considered separately. Hence, in the sequel, the superscripts r and l will be omitted and will be used explicitly only when it is required to distinguish between the right and the left arm.

The velocity of frame Σ_{f_i} with respect to the base frame can be represented by the (6×1) twist vector $\mathbf{v}_{f_i} = [\mathbf{o}_{f_i}^T \ \boldsymbol{\omega}_{f_i}^T]^T$, where $\boldsymbol{\omega}_{f_i}$ is the angular velocity, such that $\dot{\mathbf{R}}_{f_i} = \mathbf{S}(\boldsymbol{\omega}_{f_i})\mathbf{R}_{f_i}$, with $\mathbf{S}(\cdot)$ the skew-symmetric operator representing the vector product. The superscript b , denoting the base frame, has been omitted to simplify notation.

The differential kinematics equation relating the joint velocities to the velocity of frame Σ_{f_i} can be written as

$$\mathbf{v}_{f_i} = \begin{bmatrix} \mathbf{J}_{P_i}(\mathbf{q}_i) \\ \mathbf{J}_{O_i}(\mathbf{q}_i) \end{bmatrix} \dot{\mathbf{q}}_i = \mathbf{J}_{F_i}(\mathbf{q}_i) \dot{\mathbf{q}}_i, \quad (25)$$

where $\mathbf{q}_i^T = [\mathbf{q}_h^T \ \mathbf{q}_{f_i}^T]^T$ and \mathbf{J}_{F_i} is the Jacobian of the arm, ending with finger i .

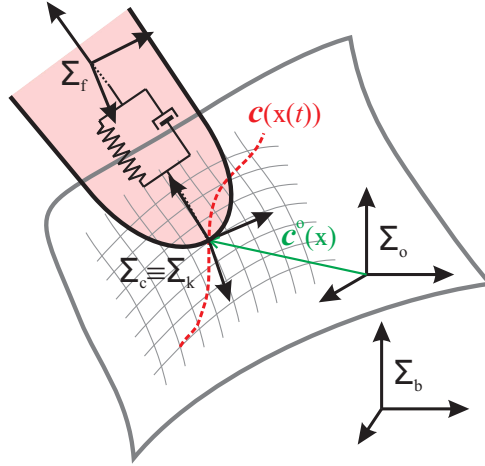


Fig. 12 Local parametrization of the object surface with respect to Σ_o

Therefore, the differential kinematics equation of the whole arm-hand system, considering the N fingers as end-effectors, can be written in the form

$$\tilde{\mathbf{v}}_f = \mathbf{J}(\mathbf{q})\dot{\mathbf{q}}, \quad (26)$$

where $\tilde{\mathbf{v}}_f^T = [\mathbf{v}_{f_1}^T \cdots \mathbf{v}_{f_N}^T]^T$, $\mathbf{q}^T = [\mathbf{q}_h^T \mathbf{q}_1^T \cdots \mathbf{q}_N^T]^T$, and \mathbf{J} is the Jacobian of the overall arm-hand system.

Assuming that the hand grasps a rigid object, to derive the kinematic mapping between the joint variables of the arm-hand system and the pose (position and orientation) of the object, it is useful introducing an object frame Σ_o attached to the object, usually chosen with the origin in the object center of mass. Let \mathbf{R}_o and \mathbf{o}_o denote respectively the rotation matrix and the position vector of the origin of Σ_o with respect to the base frame, and let \mathbf{v}_o denote the velocity twist vector.

Grasping situations may involve moving rather than fixed contacts: often, both the object and the robotic fingers are smooth surfaces, and manipulation involves rolling and/or sliding of the fingertips on the object surface, depending on the contact type. If the fingers and object shapes are completely known, the contact kinematics can be described introducing contact coordinates defined on the basis of a suitable parametrization of the contact surfaces [39], [41].

In this work, it is assumed that the fingertips are sharp (i.e. they end with a point, denoted as tip point) and covered by an elastic pad. The elastic contact is modeled by introducing a finger contact frame, Σ_{k_i} , attached to the soft pad and with the origin in the tip point \mathbf{o}_{k_i} , and a spring-damper system connecting \mathbf{o}_{k_i} with the origin of frame Σ_{f_i} , attached to the rigid part of the finger (see Fig. 12) and with the same orientation of Σ_{k_i} . The displacement between Σ_{f_i} and Σ_{k_i} , due to the elastic contact force, can be computed as

$$\mathbf{o}_{f_i} - \mathbf{o}_{k_i} = (l_i - \Delta l_i) \mathbf{R}_o \hat{\mathbf{n}}^o(\xi), \quad (27)$$

where l_i and $0 \leq \Delta l_i \leq l_i$ are the rest position and the compression of the spring, respectively, and $\hat{\mathbf{n}}^o$ is the vector representing the outward normal to the object's surface at the contact point, referred to Σ_o .

Let Σ_{c_i} be the contact frame attached to the object, with the origin at contact point \mathbf{o}_{c_i} . Notice that, instantaneously, the object contact point \mathbf{o}_{c_i} and the finger contact point \mathbf{o}_{k_i} are coincident. One of the axes of Σ_{c_i} , e.g., the Z axis, is assumed to be the outward normal to the tangent plane to the object surface at the contact point.

It is assumed that, at least locally, the position of the contact point with respect to the object frame $\mathbf{o}_{o,c_i}^o = \mathbf{o}_{c_i}^o - \mathbf{o}_o^o$ can be parameterized in terms of a coordinate chart $\mathbf{c}_i^o : U_i \subset \mathbb{R}^2 \mapsto \mathbb{R}^3$ which maps a point $\xi_i = [u_i \ v_i]^T \in U_i$ to the point $\mathbf{o}_{o,c_i}^o(\xi_i)$ of the surface of the object.

Assuming that \mathbf{c}_i^o is a diffeomorphism and that the coordinate chart is orthogonal and right-handed, the contact frame Σ_{c_i} can be chosen as a Gauss frame [39], where the relative orientation expressed by the rotation matrix $\mathbf{R}_{c_i}^o$ is computed as a function of the orthogonal tangent vectors $\mathbf{c}_{u_i}^o = \partial \mathbf{c}_i^o / \partial u_i$ and $\mathbf{c}_{v_i}^o = \partial \mathbf{c}_i^o / \partial v_i$ [31].

Consider the contact kinematics from the object point of view. Let $\mathbf{c}_i^o(\xi_i(t))$ denote a curve on the surface of the object, with $\xi_i(t) \in U$ (see Fig. 12). The corresponding motion of Σ_{c_i} with respect to the base frame can be determined as a function of: object motion, geometric parameters of the object and the curve geometric features. Namely, the velocity of the contact frame can be expressed as

$$\mathbf{v}_{c_i} = \begin{bmatrix} \dot{\mathbf{o}}_{c_i} \\ \boldsymbol{\omega}_{c_i} \end{bmatrix} = \mathbf{G}_{\xi_i}^T(\xi_i) \mathbf{v}_{o_i} + \mathbf{J}_{\xi_i}(\xi_i) \dot{\xi}_i, \quad (28)$$

where $\mathbf{G}_{\xi_i}(\xi_i)$ and $\mathbf{J}_{\xi_i}(\xi_i)$ are respectively (6×6) and (6×2) full rank matrices, whose expressions can be found in [31].

Consider now the contact kinematics from the fingers point of view. The contact can be modeled with an unactuated 3-DOF ball and socket kinematic pair centered at the origin \mathbf{o}_{k_i} of Σ_{k_i} , fixed to the soft pad of the finger; the origin may also move on the surface, if sliding is allowed. Therefore, the relative orientation $\mathbf{R}_{c_i}^{k_i}$ of Σ_{c_i} with respect to Σ_{k_i} can be computed in terms of a suitable parametrization of the ball and socket joint, e.g., Euler angles.

A vector $\theta_i = [\theta_{i1} \ \theta_{i2} \ \theta_{i3}]^T$ of XYZ Euler angles can be considered, and thus $\mathbf{R}_{c_i}^{k_i} = \mathbf{R}_{c_i}^{k_i}(\theta_i)$. Singularities occurs for $\theta_{2i} = \pm\pi/2$, but they do not correspond to physical singularities of the kinematic pair.

Notice that, in the presence of a contact force, because of the tip elasticity, frame Σ_{k_i} translates from the finger frame Σ_{f_i} according to (27), but the orientation does not change. Therefore, $\mathbf{R}_{c_i}^{k_i} = \mathbf{R}_{c_i}^{f_i}$. Moreover, the angular velocity of Σ_{c_i} relative to Σ_{f_i} can be expressed as $\boldsymbol{\omega}_{f_i,c_i}^{f_i} = \mathbf{H}(\theta_i) \dot{\theta}_i$, where \mathbf{H} is a transformation matrix depending on the joint parameterization. In view of the decomposition $\boldsymbol{\omega}_{c_i} = \boldsymbol{\omega}_{f_i} + \mathbf{R}_{f_i}(\mathbf{q}_i) \boldsymbol{\omega}_{f_i,c_i}^{f_i}$, and from (25), the angular velocity of Σ_{c_i} can be computed also as a function of joint and contact variables in the form

$$\boldsymbol{\omega}_{c_i} = \mathbf{J}_{O_i}(\mathbf{q}_i) \dot{\mathbf{q}}_i + \mathbf{R}_{f_i}(\mathbf{q}_i) \mathbf{H}(\theta_i) \dot{\theta}_i, \quad (29)$$

with \mathbf{J}_{O_i} defined in (25). Moreover, since the origins of Σ_{c_i} and Σ_{k_i} coincide, the following equalities hold:

$$\begin{aligned}\mathbf{o}_{c_i} &= \mathbf{o}_{k_i} = \mathbf{o}_{f_i} - (l_i - \Delta l_i) \mathbf{R}_o \hat{\mathbf{n}}_i^o(\xi_i) \\ \dot{\mathbf{o}}_{c_i} &= \mathbf{J}_{F_i}(\mathbf{q}_i) \dot{\mathbf{q}}_i + \dot{\Delta l}_i \mathbf{R}_o \hat{\mathbf{n}}_i^o(\xi_i) \\ &\quad + (l_i - \Delta l_i) \mathbf{S}(\mathbf{R}_o \hat{\mathbf{n}}_i^o(\xi_i)) \omega_o - (l_i - \Delta l_i) \mathbf{R}_o \frac{\partial \hat{\mathbf{n}}_i^o(\xi_i)}{\partial \xi_i} \dot{\xi}_i,\end{aligned}\quad (30)$$

with \mathbf{J}_{F_i} defined in (25). Using (29) and (30), the velocity of the contact frame can be expressed as

$$\begin{aligned}\mathbf{v}_{c_i} &= \mathbf{J}_{F_i}(\mathbf{q}) \dot{\mathbf{q}} + \mathbf{J}_{\theta_i}(\theta_i, \mathbf{q}_i) \dot{\theta}_i + \mathbf{J}_{\Delta l_i}(\xi_i) \dot{\Delta l}_i \\ &\quad - \mathbf{J}'_{\xi_i}(\xi_i, \Delta l_i) \dot{\xi}_i - \mathbf{G}_{\Delta l_i}^T(\xi_i, \Delta l_i) \mathbf{v}_o,\end{aligned}\quad (31)$$

where \mathbf{J}_{θ_i} is a (6×3) full rank matrix, whose detailed expression can be found in [31], $\mathbf{J}_{\Delta l_i}$ is a (6×1) vector

$$\mathbf{J}_{\Delta l_i} = \begin{bmatrix} \mathbf{R}_o \hat{\mathbf{n}}_i^o(\xi_i) \\ \mathbf{0} \end{bmatrix},$$

\mathbf{J}'_{ξ_i} is a (6×2) full rank matrix

$$\mathbf{J}'_{\xi_i} = \begin{bmatrix} (l_i - \Delta l_i) \mathbf{R}_o \frac{\partial \hat{\mathbf{n}}_i^o(\xi_i)}{\partial \xi_i} \\ \mathbf{0} \end{bmatrix},$$

and $\mathbf{G}_{\Delta l_i}$ is the (6×6) matrix

$$\mathbf{G}_{\Delta l_i} = \begin{bmatrix} \mathbf{0} & \mathbf{0} \\ (\Delta l_i - l_i) \mathbf{S}(\mathbf{R}_o \hat{\mathbf{n}}_i^o(\xi_i)) & \mathbf{0} \end{bmatrix}.$$

Hence, from (28) and (31), the contact kinematics of finger i has the form

$$\mathbf{J}_{F_i}(\mathbf{q}_i) \dot{\mathbf{q}}_i + \mathbf{J}_{\eta_i}(\eta_i, \mathbf{q}_i, \Delta l_i) \dot{\eta}_i + \mathbf{J}_{\Delta l_i}(\xi_i) \dot{\Delta l}_i = \mathbf{G}_i^T(\eta_i, \Delta l_i) \mathbf{v}_o, \quad (32)$$

where $\eta_i = [\xi_i^T \ \theta_i^T]^T$ is the vector of contact variables, $\mathbf{J}_{\eta_i} = [-(\mathbf{J}_{\xi_i} + \mathbf{J}'_{\xi_i}) \ \mathbf{J}_{\theta_i}]$ is a (6×5) full rank matrix, and $\mathbf{G}_i = \mathbf{G}_{\xi_i} + \mathbf{G}_{\Delta l_i}$ is a (6×6) full rank grasp matrix. This equation can be interpreted as the differential kinematics equation of an “extended” finger corresponding to the kinematic chain including the arm and finger joint variables (active joints) and the contact variables (passive joints), from the base frame to the contact frame [40].

It is worth noticing that equation (32) involves all the 6 components of the velocity, differently from the grasping constraint equation usually considered (see, e.g., [41]), which contains only the components of the velocities that are transmitted by the contact. The reason is that the above formulation takes into account also the

velocity components not transmitted by contact i , parameterized by the contact variables and lying in the range space of $[\mathbf{J}_{\eta_i} \ \mathbf{J}_{\Delta l_i}]$. As a consequence, \mathbf{G}_i is always a full-rank matrix.

Depending on the considered contact type [49], some of the parameters of ξ_i and θ_i are constant. Hence, assuming that the contact type remains unchanged during the task, the variable parameters at each contact point are grouped in an $(n_{c_i} \times 1)$ vector η_i of contact variables, with $n_{c_i} \leq 5$.

Differently from the classical grasp analysis, in this work the elasticity of the soft pad has been explicitly modeled (although using a simplified model). This means that the force along the normal to the contact surface is always of elastic type. The quantity Δl_i , at steady state, is related to the normal contact force f_{ni} by the equation $\Delta l_i = f_{ni}/k_i$, being k_i the elastic constant of the soft pad of finger i .

Object dynamic manipulation is, in general, a difficult task, since the number of the control variables (the active joints) is lower than the number of configuration variables (active and passive joints). However, in some particular situations, it is possible to simplify the analysis, considering only the kinematics of the system.

To this purpose, assume that force sensors are available on the fingertips and a force control strategy is employed to ensure a desired constant contact forces f_{di} along the direction normal to the contact point. Therefore, $\Delta l_i = \Delta l_{di} = f_{di}/k_i$ can be assumed to be fixed ($\dot{\Delta l}_i = 0$) and equation (32) can be rewritten as

$$\mathbf{J}_{F_i}(\mathbf{q}_i)\dot{\mathbf{q}}_i + \mathbf{J}_{\eta_i}(\eta_i, \mathbf{q}_i, \Delta l_i)\dot{\eta}_i = \mathbf{G}_i^T(\eta_i, \Delta l_i)\mathbf{v}_o. \quad (33)$$

On the basis of (33), it is possible to make a kinematic classification of the grasp [49].

A grasp is *redundant* if the null space of the matrix $[\mathbf{J}_{F_i} \ \mathbf{J}_{\eta_i}]$ is non-null, for at least one finger i . In this case, the mapping between the joint variables of “extended” finger i and the object velocity is many to one: motions of active and passive joints of the extended finger are possible when the object is locked.

A grasp is *indeterminate* if the intersection of the null spaces of $[-\mathbf{J}_{\eta_i} \ \mathbf{G}_i^T]$, for all $i = 1, \dots, N$, is non-null. In this case, motions of the object and of the passive joints are possible when the active joints of all the fingers are locked.

It is worth noticing that, also in the case of redundant and indeterminate grasps, for a given object pose and fingers configuration, the value of the contact variables is uniquely determined. More details can be found in [31].

2.2 Control Scheme With Redundancy Resolution

In the case of a kinematically determinate and, possibly, redundant grasp, a two-stage control scheme is proposed for the dual arm-hand manipulation system. The first stage is an inverse kinematics scheme with redundancy resolution, which computes the joint references for the active joints corresponding to a desired object’s motion —assigned in terms of the homogeneous transformation matrix \mathbf{T}_d and the

corresponding twist velocity vector \mathbf{v}_{o_d} — and to the desired normal contact force $\mathbf{f}_d^T = [f_{d1} \cdots f_{dN}]$. The second stage is a parallel control composed of a PD position controller and a PI tip force controller, ensuring the desired object motion and desired contact forces on the basis of the previously computed joint references.

Namely, in ideal conditions, the joint references computed by the kinematic stage ensure tracking of the desired object motion, with the desired contact forces. In the presence of modeling errors and parameters uncertainty, the contact forces may differ from those planned. Using the force sensors at the fingertips, a force control strategy is adopted to ensure the desired contact force by modifying the joint references computed by the inverse kinematics stage. In principle, the joint references of the overall manipulation system could be involved; however, it is reasonable to design a force controller acting only on the joints of the fingers.

In order to derive the equations of the first stage, starting from (32), it is useful to write the differential kinematic equations of the whole (right or left) arm-hand system as

$$\mathbf{J}(\mathbf{q})\dot{\mathbf{q}} + \mathbf{J}_\eta(\eta, \mathbf{q}, \Delta\mathbf{l})\dot{\eta} = \mathbf{G}^T(\eta, \Delta\mathbf{l})\tilde{\mathbf{v}}_o, \quad (34)$$

where \mathbf{J} is the Jacobian of the arm-hand system defined in (26), \mathbf{J}_η is a block diagonal matrix $\mathbf{J}_\eta = \text{diag}\{\mathbf{J}_{\eta_1}, \dots, \mathbf{J}_{\eta_N}\}$ corresponding to the vector of passive joints $\eta^T = [\eta_1^T \cdots \eta_N^T]^T$, \mathbf{G} is the block diagonal grasp matrix $\mathbf{G} = \text{diag}\{\mathbf{G}_1, \dots, \mathbf{G}_N\}$, $\Delta\mathbf{l}^T = [\Delta l_1 \cdots \Delta l_N]^T$ and $\tilde{\mathbf{v}}_o^T = [\mathbf{v}_o^T \cdots \mathbf{v}_o^T]^T$.

From (34), the following closed-loop inverse kinematics algorithm can be derived:

$$\begin{bmatrix} \dot{\mathbf{q}}_d \\ \dot{\eta}_d \end{bmatrix} = \tilde{\mathbf{J}}^\dagger(\mathbf{q}_d, \eta_d, \Delta\mathbf{l}_d)\mathbf{G}^T(\tilde{\mathbf{v}}_{o_d} + \mathbf{K}_o\tilde{\mathbf{e}}_o) + \mathbf{N}_o\sigma, \quad (35)$$

where $\tilde{\mathbf{J}} = [\mathbf{J} \ \mathbf{J}_\eta]$, the symbol \dagger denotes a right (weighted) pseudo-inverse, $\tilde{\mathbf{v}}_{o_d}^T = [\mathbf{v}_{o_d}^T \cdots \mathbf{v}_{o_d}^T]^T$, \mathbf{K}_o is a diagonal and positive definite matrix gain, $\tilde{\mathbf{e}}_o^T = [\mathbf{e}_{o_1}^T \cdots \mathbf{e}_{o_N}^T]^T$, being \mathbf{e}_{o_i} the pose error between the desired and the current object pose computed on the basis of the direct kinematics of the extended finger i , and $\mathbf{N}_o = \mathbf{I} - \tilde{\mathbf{J}}^\dagger\tilde{\mathbf{J}}$ is a projector in the null space of the Jacobian matrix $\tilde{\mathbf{J}}$. The quantity $\Delta\mathbf{l}_d$ in (35) is the vector collecting the finger soft pad deformations $\Delta l_{di} = f_{di}/k_i$ corresponding to the desired contact force f_{di} .

Equation (35) is used to compute the joint reference vector \mathbf{q}_d for the controller of the second stage.

In view of the above considerations, any kind of joint motion control can be adopted for the arms of the bimanual manipulation system, receiving as input the joint references computed by the inverse kinematics scheme. In this chapter, the joint torques for finger i are set according to the parallel force/position control law

$$\tau_i = \mathbf{J}_i^T(\mathbf{q}_i) \left(k_P \Delta \mathbf{p}_i + \mathbf{f}_{di} + k_F \Delta \mathbf{f}_{ni} + k_I \int_0^t \Delta \mathbf{f}_{ni} d\tau \right) - k_d \dot{\mathbf{q}}_i + \mathbf{g}_i(\mathbf{q}_i) \quad (36)$$

where $\mathbf{g}_i(\mathbf{q}_i)$ is the vector of the gravity torque of finger i , $\Delta \mathbf{p}_i$ denotes the position error of finger i between the desired value computed through direct kinematics starting from \mathbf{q}_{d_i} and the current one, and $\Delta \mathbf{f}_{ni}$ is the projection of the force error along the normal to the object surface at the contact point. The above control law regulates the contact force to the desired value at the expense of a position error (i.e., a displacement of the positions of the fingers with respect to the palm), in the presence of uncertainties.

Since the system may be highly redundant, multiple tasks could be fulfilled, provided that they are suitably arranged in a priority order, according to the *augmented projection method* [1]. Consider m secondary tasks, each expressed by a task function $\sigma_{t_h}(\tilde{\mathbf{q}})$ ($h = 1, \dots, m$), where $\tilde{\mathbf{q}} = [\mathbf{q}_d^T \eta_d^T]^T$. According to the *augmented projection method* [1], the control law (35) can be replaced by

$$\dot{\tilde{\mathbf{q}}} = \tilde{\mathbf{J}}^\dagger(\tilde{\mathbf{q}}, \Delta \mathbf{l}_d) \mathbf{G}^T(\tilde{\mathbf{v}}_{o_d} + \mathbf{K}_o \tilde{\mathbf{e}}_o) + \sum_{h=1}^m \mathbf{N}(\mathbf{J}_{t_h}^A) \mathbf{J}_{t_h}^\dagger \mathbf{K}_{t_h} \mathbf{e}_{t_h}, \quad (37)$$

where \mathbf{J}_{t_h} is the Jacobian of the h th task, $\mathbf{J}_{t_h}^A$ is the augmented Jacobian, given by

$$\mathbf{J}_{t_h}^A(\tilde{\mathbf{q}}, \Delta \mathbf{l}_d) = \left[\tilde{\mathbf{J}}^T(\tilde{\mathbf{q}}, \Delta \mathbf{l}_d) \mathbf{J}_{t_1}^T(\tilde{\mathbf{q}}) \dots \mathbf{J}_{t_{h-1}}^T(\tilde{\mathbf{q}}) \right]^T.$$

$\mathbf{N}(\mathbf{J}_{t_h}^A)$ is a null projector of the matrix $\mathbf{J}_{t_h}^A$, \mathbf{K}_{t_h} is a positive definite gain matrix and $\mathbf{e}_{t_h} = \sigma_{t_{hd}} - \sigma_{t_h}$ is the task error, being $\sigma_{t_{hd}}$ the desired value of the h -th task variable.

The augmented projection method can be also adopted to fulfill mechanical or environmental constraints, such as joint limits and obstacle avoidance (other fingers or the grasped object). To this aim, each constraint can be described by means of a cost function, $\mathcal{C}(\tilde{\mathbf{q}})$, increasing when the manipulator comes close to violate the constraint. In order to minimize the cost function, the manipulator could be moved according to the opposite of the gradient $-\nabla_{\tilde{\mathbf{q}}}^T \mathcal{C}(\tilde{\mathbf{q}})$, that could be considered as a fictitious force moving the manipulator away from configurations violating the constraints. In order to include the constraints in (37), an overall cost function \mathcal{C}_Σ given by

$$\mathcal{C}_\Sigma(\tilde{\mathbf{q}}) = \sum_{c_s} \gamma_{c_s} \mathcal{C}_{c_s}(\tilde{\mathbf{q}}), \quad (38)$$

is introduced, where γ_{c_s} and \mathcal{C}_{c_s} are a positive weight and a cost function, respectively, referred to the c_s th constraint.

2.3 Task Sequencing

If the system comes close to violate a constraint, a high level supervisor has to remove some secondary tasks and relax enough DOFs to fulfill the constraint [36]. To manage in a correct way removal/insertion of tasks from/into the stack (task

sequencing), a suitable task supervisor can be designed, based on a three layers architecture: the lower layer computes the motion variables on the basis of a stack of active tasks; the intermediate layer determines which tasks must be removed from the stack in order to respect the constraints; the upper layer verifies if the previously removed tasks can be pushed back in the stack.

A task must be removed from the stack when the predicted value of the overall cost function at the next time step is above a suitable defined threshold, $\overline{\mathcal{C}}$. Let T be the sampling time adopted to implement the control law and κT the actual time, the configuration at time instant $(\kappa + 1)T$ can be estimated as follows

$$\widehat{\mathbf{q}}(\kappa + 1) = \widetilde{\mathbf{q}}(\kappa) + T\dot{\widetilde{\mathbf{q}}}(\kappa). \quad (39)$$

Hence, a task must be removed from the stack if

$$\mathcal{C}_\Sigma(\widehat{\mathbf{q}}(\kappa + 1)) \geq \overline{\mathcal{C}}. \quad (40)$$

Once it has been ascertained that a task must be removed from the stack, the problem is to detect which task has to be removed. To the purpose, several criteria have been proposed in [36], with the aim of verifying the conflict between the constraints and each task. In this chapter, the overall cost function gradient is projected in the null space of the task Jacobian, i.e.,

$$\mathcal{P}_h = \left\| \mathbf{N}(\mathbf{J}_{t_h}) \left(-\nabla_{\mathbf{q}}^T \mathcal{C}_\Sigma \right) \right\| \quad h = 1, \dots, m; \quad (41)$$

the task corresponding to the minimum of \mathcal{P}_h is then removed, since its projection into the null-space of \mathbf{J}_{t_h} should be, ideally, zero to ensure constraint fulfillment.

The tasks removed by the second layer must be reinserted in the stack as soon as possible, provided that the constraints will not be violated. A prediction of the \mathcal{C}_Σ evolution at the next time step has to be evaluated by considering the effect of each task currently out of the stack, i.e.

$$\widehat{\mathbf{q}}_{t_h}(\kappa + 1) = \widetilde{\mathbf{q}}(\kappa) + \mathbf{J}_{t_h}^\dagger \mathbf{e}_{t_h}(\kappa). \quad (42)$$

Therefore, let $\underline{\mathcal{C}} < \overline{\mathcal{C}}$ be a suitably chosen threshold; a task is pushed back in the stack if

$$\mathcal{C}_\Sigma(\widehat{\mathbf{q}}_{t_h}(\kappa + 1)) \leq \underline{\mathcal{C}}. \quad (43)$$

Task sequencing might cause discontinuities in the commanded joint velocities due to the change of active tasks in the stack. For each task a variable gain ρ_{t_h} is introduced to achieve a smooth behavior of the controller output

$$\rho_{t_h}(t) = \begin{cases} 1 - e^{-\mu(t-\tau)} & \text{if the } h\text{-th task is in the stack} \\ e^{-\mu(t-\tau')} & \text{if the } h\text{-th task is out of the stack,} \end{cases}$$

where τ and τ' are the time instant in which the task is inserted in the stack and the time instant in which it is removed, respectively, and $1/\mu$ is a time constant.

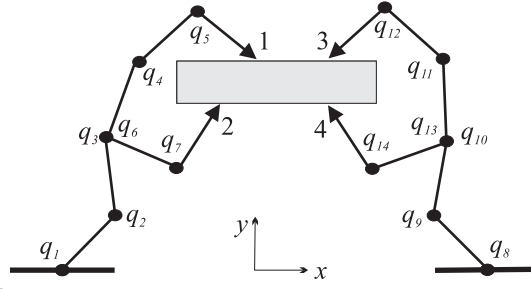


Fig. 13 Manipulation system.

Hence, the first stage control law can be written in its complete form

$$\ddot{\tilde{\mathbf{q}}} = \tilde{\mathbf{J}}^\dagger(\tilde{\mathbf{q}}, \Delta \mathbf{I}_d) \mathbf{G}^T (\tilde{\mathbf{v}}_{o_d} + \mathbf{K}_o \tilde{\mathbf{e}}_o) + \sum_{h=1}^m \rho_{t_h} \mathbf{N}(\mathbf{J}_{t_h}^A) \mathbf{J}_{t_h}^\dagger \mathbf{K}_{t_h} \mathbf{e}_{t_h} - k_\nabla \mathbf{N}(\mathbf{J}_{t_{m+1}}^A) \nabla_{\tilde{\mathbf{q}}}^T \mathcal{L}_\Sigma,$$

where k_∇ is a positive gain.

2.4 Case Study

The presented control scheme has been tested on a manipulation system grasping a certain object, represented in Fig. 13, composed by two identical planar grippers, each with two branches and 7 DOFs, resulting in a total of $N = 4$ fingers and 14 active joints. The idea is that of performing an object exchange.

In its initial configuration, it is assumed that the system grasps the object with only tips 1 and 2, which are in a force closure condition, since the contact normal forces are acting on the same straight line [41]. Tips 3 and 4 approach the object until they reach a condition in which all the tips are in contact with the object. The main task consists in keeping the object still, while Tips 3 and 4 move in order to achieve a force closure condition upon the object in a dexterous configuration, without violating a certain number of limits and constraints. Then, Fingers 1 and 2 can leave the object, simulating in this way an hand-to-hand object passing.

The force control loop ensures that the planned forces are applied on the object. In this case study, the desired forces for Tips 3 and 4 are negligible, since they have to slide on the object's surface so as to reconfigure themselves to reach force closure condition. The desired forces for Tips 1 and 2 are dynamically planned, on the basis of the current value of the forces exerted by the fingers, in order to produce zero net force and moment on the object and to balance disturbances caused by movements of the other two fingertips.

A sequence of snapshots representing the described task are shown in Fig. 14. It can be noticed that, in the final configuration (fifth snapshot), Fingers 3 and 4 are in a force closure condition, since the normals at the contact points act on the same straight line.

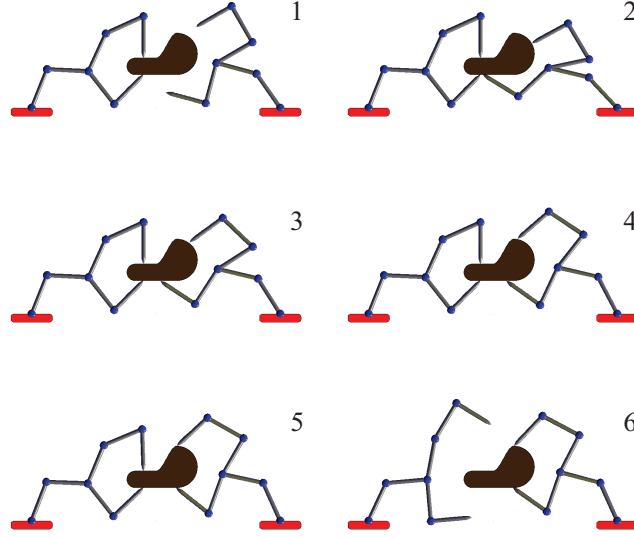


Fig. 14 Snapshots describing the case study.

Four different subtasks have been considered: the first two, aimed at choosing the optimal contact points, are related to the grasp quality; the others regard the manipulability and the distance between the palm and the grasped object.

Unit frictionless equilibrium. The grasp quality can be guaranteed by moving the contact points on the object surface until the unit frictionless equilibrium is reached. This condition is a special case of a force-closure grasp; it is satisfied when two positive indices, called frictionless force (ε_f) and moment (ε_m) residuals, are zero: [16], [45]

$$\varepsilon_f = \frac{1}{2} \mathbf{f}^T \mathbf{f} \quad \mathbf{f} = \sum_{i=1}^4 \hat{\mathbf{n}}_i^o \quad (44)$$

$$\varepsilon_m = \frac{1}{2} \mathbf{m}^T \mathbf{m} \quad \mathbf{m} = \sum_{i=1}^4 \mathbf{c}_i^o \times \hat{\mathbf{n}}_i^o, \quad (45)$$

where $i = 1, \dots, 4$, and where $\hat{\mathbf{n}}_i^o(\xi_i)$ and $\mathbf{c}_i^o(\xi_i)$ are the surface normal and the position of the i th contact point, respectively, both referred to the object frame. It has been shown that, for two or more contact points, unit frictionless equilibrium is a force closure condition for any nonzero friction coefficient [45], [46].

Manipulability. In order to keep the manipulator far from singularities, a manipulability index of each finger can be considered. In detail, the following manipulability measure, which vanishes at a singular configuration, is adopted for the i -th finger [55]

$$w_i(q_i) = \sqrt{\det(J_i(q_i)J_i^T(q_i))} \quad i = 1, \dots, 4. \quad (46)$$

The considered task function is then

$$\sigma_{w_i} = \begin{cases} \frac{1}{2}(\bar{w}_i - w_i(q_i))^2 & \text{if } w_i(q_i) < \bar{w}_i \\ 0 & \text{otherwise,} \end{cases} \quad (47)$$

where \bar{w}_i is a threshold for the task activation. The desired value, $\sigma_{w_i d}$, is zero.

Distance between palm and object. Consider the position \mathbf{p}_c^o of the palm centroid in the object frame and a suitably chosen surface \mathcal{S} surrounding the object characterized by the equation $\mathcal{F}(\mathbf{p}^o) = 0$. When the centroid is inside the surface \mathcal{S} , a collision can occur; therefore, the centroid must be moved on the boundary, i.e., in a position such that $\mathcal{F}(\mathbf{p}_c^o) = 0$. Hence, the task function is the following

$$\sigma_P(p_c^o) = \begin{cases} \mathcal{F}(p_c^o) & \text{if the centroid is inside } \mathcal{S} \\ 0 & \text{otherwise.} \end{cases} \quad (48)$$

In the following the two considered constraints are described.

Joint-limit avoidance. A physical constraint to the motion of the system is imposed by the mechanical joint limits. The system configuration is considered safe if $q_j \in [\underline{q}_j, \bar{q}_j]$, for $j = 1, \dots, 14$, with \underline{q}_j and \bar{q}_j suitable chosen values far enough from the limits. The cost function, directly defined in the joint space, is the following:

$$\mathcal{C}_{JL}(\mathbf{q}) = \sum_{j=1}^{14} c_j(q_j), \quad (49)$$

$$c_j(q_j) = \begin{cases} k_j e^{\delta(q_j - \underline{q}_j)^2} - 1 & \text{if } q_j \leq \underline{q}_j \\ 0 & \text{if } \underline{q}_j < q_j \leq \bar{q}_j \\ k_j e^{\delta(q_j - \bar{q}_j)^2} - 1 & \text{if } q_j > \bar{q}_j, \end{cases}$$

where k_j and δ are positive constants.

Collision avoidance. In order to avoid collisions between the fingers, it is imposed that the distance between the fingers be larger than a safety value, d_s ; hence, if $d_{ii'}$ denotes the distance between the i th and the i' th finger, the following cost function can be formalized

$$\mathcal{C}_{CA}(\tilde{\mathbf{q}}) = \sum_{i,i'} c_{ii'}(\tilde{\mathbf{q}}), \quad (50)$$

where the sum is extended to all the couples of fingers,

$$c_{ii'}(d_{ii'}) = \begin{cases} k_{ii'} \frac{d_s - d_{ii'}}{d_{ii'}^2} & \text{if } d_{ii'} \leq d_s \\ 0 & \text{if } d_{ii'} > d_s, \end{cases} \quad (51)$$

and $k_{ii'}$ is a positive gain.

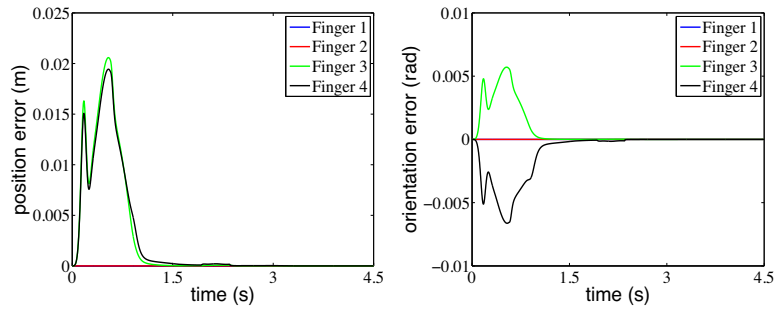


Fig. 15 Object's pose errors for each finger.

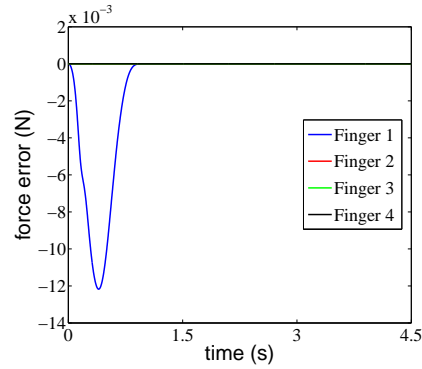


Fig. 16 Finger force errors.

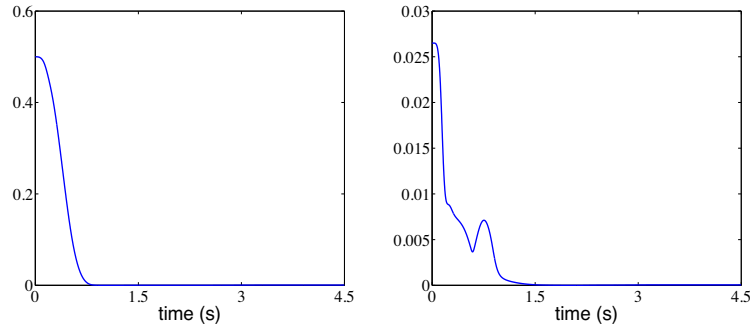


Fig. 17 Force and moment residuals.

The parameters of the elastic contact are: $5 \cdot 10^4$ N/m for the springs elastic coefficients, $5 \text{ N s}^2 / \text{m}$ for the springs damper coefficients and $l_i = 5 \cdot 10^{-3}$ m for the springs rest condition. The parameters used to define the subtasks are chosen as follows: $\bar{w}_i = 2.55$ for the manipulability subtask, $\underline{q}_j = -110^\circ, \bar{q}_j = 110^\circ, k_j = 5, \delta = 2$ for the joint-limit avoidance and $k_{ii'} = 1, d_s = 5$ cm for the collision avoidance. In the system of Fig. 13 the palm is represented by the ramification point of the right manipulator. The task has a duration of 4.5 s; a Runge-Kutta integration method, with a step size of 2 ms, has been used to simulate the system.

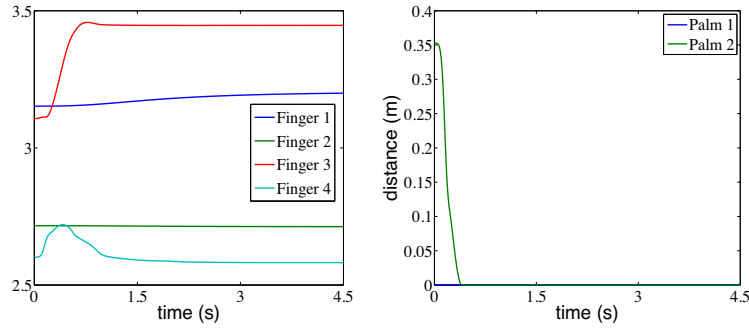


Fig. 18 Subtask functions.

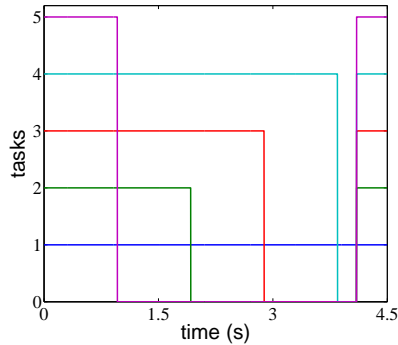


Fig. 19 Time history of the stack status: 1 is the main task, corresponding to keep the object fixed; 2 and 3 are the force and moment residual tasks, respectively; 4 is the manipulability task; 5 is the task about the distance between palms and object.

Figure 15 shows the time history of the norm of the object's pose error for each finger (position on the left, orientation on the right). Figure 16 shows the evolution of the force error for each finger: in detail, Finger 1 is much more affected by the motion of Fingers 3 and 4 than that of Finger 2; the desired value for the normal force at Tips 3 and 4 is very small and it is impossible to see remarkable variations in the time history.

Figure 17 shows the force and moment residuals, ε_f and ε_m , respectively. Since both residuals asymptotically converge to zero, it is clear that Fingers 3 and 4 reach a force closure condition.

Figure 18 shows the time history of the manipulability measure (left) and the distance from the palm function σ_P in (48) (right). The manipulability measure of each finger is above the limit value \bar{w}_i , while σ_P is zero when the task is not activated, since the palm is sufficiently far from the object.

Finally, Figure 19 depicts the time history of the stack status during the simulation. It can be noticed that the main task is never removed from the stack, while the other tasks are removed when some constraints are near to be violated. When the system is in a safe condition with respect to the constraints, the tasks are re-inserted

in the stack maintaining their previous priorities. Notice that the label assigned at each task denotes its priority in the stack.

3 Control Using Postural Synergies

Recent works on the application of human hand postural synergies to a robotic hand demonstrate that understanding human prehension is a promising way to simplify and optimize the control of multiple-DOF limbs. In order to interact with humans directly, the robots of the future will require enhanced manipulation capabilities similar to those of human beings. For this purpose, complex dexterous hands with advanced sensorimotor skills and human-like kinematics are needed. The human hand is an excellent example of dexterous bio-mechanical architecture with versatile capabilities to perform different kinds of tasks. The undergoing research in the field aims at the reproduction of human's abilities not only by means of anthropomorphic design but also by the adoption of human-inspired control strategies. To this purpose postural synergies have been identified to be the key strategies in planning and control of the robotic and prosthetic hands of the future.

The studies on grasp taxonomy carried out by scientists such as Napier [42], Cutkosky [17] and Iberall [29] aim at defining which fingers (and which parts of the fingers) are used by humans to generate forces on the grasped object. According to this classification, the hand configuration during grasping operation can be decomposed in a limited set of basic postures. On the other hand, recent advances in neuroscience have shown that control of the human hand during grasping is dominated by movements in a continuous configuration space of highly reduced dimensionality with respect to the number of DOFs [52], [37].

In this work, the eigengrasps of the DEXMART Hand (Fig. 1) have been derived using the principal component analysis (PCA) by considering a set of 36 hand configurations among precision, intermediate and power grasps of common (for humans) objects contained in a comprehensive human grasp taxonomy [51]. A method is proposed to derive the postural synergies of the DEXMART Hand from experiments and the kinematic patterns connected to the three predominant eigenpostures. Moreover, the temporal variation of the three synergies weights is exploited for real-time execution of the grasps.

From the data analysis it can be argued that the introduction of the third predominant synergy significantly improves the grasp synthesis and performance, especially with regard to the improvement of the adduction/abduction motion of the thumb. Experimental results show that grasp planning and control of the DEXMART Hand performed by using the three predominant postural synergies allows not only reproducing the set of postures adopted to derive the eigengrasps with a high level of fidelity, but also synthesizing and performing a wide set of grasps, namely precision, intermediate and power grasps of objects with different shapes and dimensions. Indeed, in order to prove the efficiency of the method, the synthesis of new grasp/object pairs not contained in the reference set of postures used for PCA has

been realized. The intent here is to imitate the typical attitude of humans in manipulation as well as to cover the entire grasp variety in recently proposed taxonomies, e.g. [20]. All the data from experiments are obtained using a prototype of the DEX-MART Hand without sensors. Thus, the motivation of this study is to test the method for deriving synergies and the potential of the anthropomorphic design of the DEX-MART Hand to work efficiently in a synergies based framework for grasp planning and prehension control during reach to grasp.

3.1 Related Work

Recently, the studies on kinematic synergies have collected the interest of many researchers not only belonging to the field of neuroscience but also working on control theory and mechanical design of artificial hands. Preliminary studies on the human hand had pointed out that the combination of tendon coupling and muscle activation patterns exhibited by humans lead to significant joint coupling and inter-finger coordination, or, in other words, to postural synergies, that are evidence of simplified control schemes occurring at neurological level for the organization of the hand movements.

In [52] the PCA has been used to calculate the postural synergies from real-world data collected on a variety of human hand postures by means of a data glove. Moreover, the authors show that a wide set of hand postures during grasping operation evolves continuously within a linear space spanned by few postural synergies that account for most of the hand configurations variance, without distinguishing between power and precision grasps. In [37] it is shown that even if higher principal components account for a small percentage of the variance, they give critical details not only for the static grasp when the hand adapts to the object shape, but also for the act of preshaping during the grasp. In [15], [13], [14] the authors extend the concept of postural synergies to robotic hands showing how a similar dimensionality reduction can be used to derive comprehensive planning and control algorithms that produce stable grasps for a number of different robot hand models. Synergies have been used to solve the dimensionality reduction problem in control and coordination of a 16-DOF underactuated prosthetic hand prototype (CyberHand), in order to perform the three prehensile forms mostly used in activities of daily living [38].

Other applications have been made in order to simplify the design and analysis of robotic hand structures [10]. In [47] the authors investigate how the number and types of synergies are related to the possibility of controlling the contact forces and the object motion in grasping and manipulation tasks. In [22], using the definition of force-closure for underactuated hands and the definition of grasping force optimization, the authors investigate the role of different postural synergies in the ability of obtaining force closure grasps and the quality of the grasps in two case studies addressing a precision and a power grasp. The manipulability analysis has been extended to synergy-actuated hands, where compliance is utilized in order to solve the force distribution problem [48]. The authors introduce new manipulability

indices which take into account underactuation and compliance. A modified model of synergies including the mechanical compliance of the hand's musculotendinous system has been proposed in [7] in order to account in the synergy model for the force distribution in the actual grasp. In [59] a synergy impedance controller has been derived and implemented on the DLR hand.

Recent work on mapping synergies from the human hand to the robot hand has been addressed in [24]. The proposed mapping strategy between the synergies of a paradigmatic human hand and a robotic hand is carried out in the task space and it is based on the use of a virtual sphere. This approach has the advantages to be independent of the robotic hand and depends only on the specific operation, and thus it can be used for robotic hands with very dissimilar kinematics. In [23] three synergies from data on human grasping experiments have been extracted and mapped to a robotic hand. Then a neural network with the features of the objects and the coefficients of the synergies has been trained and employed to control robot grasping. Neural networks have been utilized also in other papers in order to simulate temporal coordination of human reaching and grasping. In [57] the neural network model includes a synergistic control of the whole fingers during prehension and the design of a library of hand gestures.

3.2 Postural Synergies of the DEXMART Hand

Postural synergies describe patterns occurring at the joint displacement level. In [52], the authors measure a set of static human hand postures by recording 15 joint angles and, by means of the PCA, they show that the first two principal components account for $>80\%$ of the hand postures. Thus the use of the principal components, also called postural synergies, holds great potential for robot hands control, implying a substantial reduction of the grasp synthesis problem dimension with respect to the case of considering the entire number of DOFs of the robotic hand.

Drawing inspiration from the studies on the human hand motion, and since the DEXMART Hand presents human-like kinematics, we have found a set of principal components of the DEXMART Hand configuration space. The study of the two predominant synergies of the DEXMART Hand was carried out in [21], where experimental results showed that it is possible to obtain grasp synthesis for a large set of objects in the case of both precision and power grasps.

More recently, the third synergy has been experimentally obtained and evaluated. It has been shown that, by exploiting the third synergy, the movement of adduction/abduction of the thumb covers the whole range of joint limits without violating the limits of the other joints. This improves the correct opposition of the thumb and allows synthesizing and executing more precisely complex grasps and reproducing the set of postures adopted to derive the eigengrasps with higher accuracy with respect to the case in which only two synergies are used.

The first two synergies found for the DEXMART Hand account for $>77\%$ of the hand postures, thus matching quite well the results reported in [52]. Therefore, since

the three predominant postural synergies account for >85% of the hand postures, a robot hand control strategy that uses also the third synergy will significantly improve the grasping performance, as experiments reported in this work show.

The DEXMART Hand kinematics is rather close to that of the human hand. Hence, with the aim of deriving the PCA, a set of grasps similar to those illustrated in [51] has been considered. The choice of the reference set of postures has been made by taking into account all the most common human grasps considered in the grasp taxonomy literature. This set is composed of grasps of objects such as spheres of different dimensions involving a different number of fingers in both power and precise grasp configuration. Cylindrical grasps have been considered as well, distinguishing also between different positions of the thumb. Moreover, several configurations for precise grasps with index and thumb opposition as well as intermediate side grasps have been included. Following the taxonomy adopted in [20], a comprehensive hierarchical human grasp classification used for the PCA is reported in Fig. 20. Furthermore, a suitable number of open-hand configurations with different positions of the thumb and of the adduction/abduction fingers joint has been added in order to find synergies that allow the hand to moves continuously also toward open-hand configurations which are equally important to reach and grasp the objects. A total amount of $n = 36$ hand configurations have been evaluated to derive the fundamental eigenpostures. Each grasp configuration of the reference set of postures has been experimentally reproduced with the DEXMART Hand as close as possible to a natural human-like grasp, and the vector $\mathbf{c}_i \in \mathbb{R}^{15}$ of the joint angle values corresponding to each reproduced grasp has been measured. Once the set of the DEXMART Hand configurations matrix $\mathbf{C} = \{\mathbf{c}_i \mid i = 1 \dots n\}$ has been built, the vector $\bar{\mathbf{c}}$ representing the mean hand position in the grasp configurations space (zero-offset position) and the matrix $\mathbf{F} = \{\mathbf{c}_i - \bar{\mathbf{c}} \mid i = 1 \dots n\}$ of the grasp offsets with respect to the mean configuration have been computed. The PCA has then been performed on \mathbf{F} and a base matrix \mathbf{E} of the postural synergies subspace has been found. The PCA can be performed by diagonalizing the covariance matrix of \mathbf{F} as

$$\mathbf{F}\mathbf{F}^T = \mathbf{E}\mathbf{S}^2\mathbf{E}^T. \quad (52)$$

The $(h \times h)$ orthogonal matrix \mathbf{E} gives the directions of variance of the data, and the diagonal matrix \mathbf{S}^2 is the variance in each direction sorted in decreasing magnitude, i.e. the element on the diagonal represents the eigenvalue of the covariance matrix.

To verify the effectiveness of the synergy-based modeling approach, the percentage σ of the total variance of the data described by the first j -th principal components can be obtained by means of the following equation

$$\sigma_j = \sum_{k=0}^j \mathbf{s}_k / \sum_{k=0}^{15} \mathbf{s}_k \quad (53)$$

where \mathbf{s}_k is the k -th element of the diagonal of the matrix \mathbf{S}^2 . Since the three principal components account for >85% of the postures ($\sigma_3 = 0.8503$), the posture matrix \mathbf{C} can be reconstructed with good accuracy by adopting the matrix

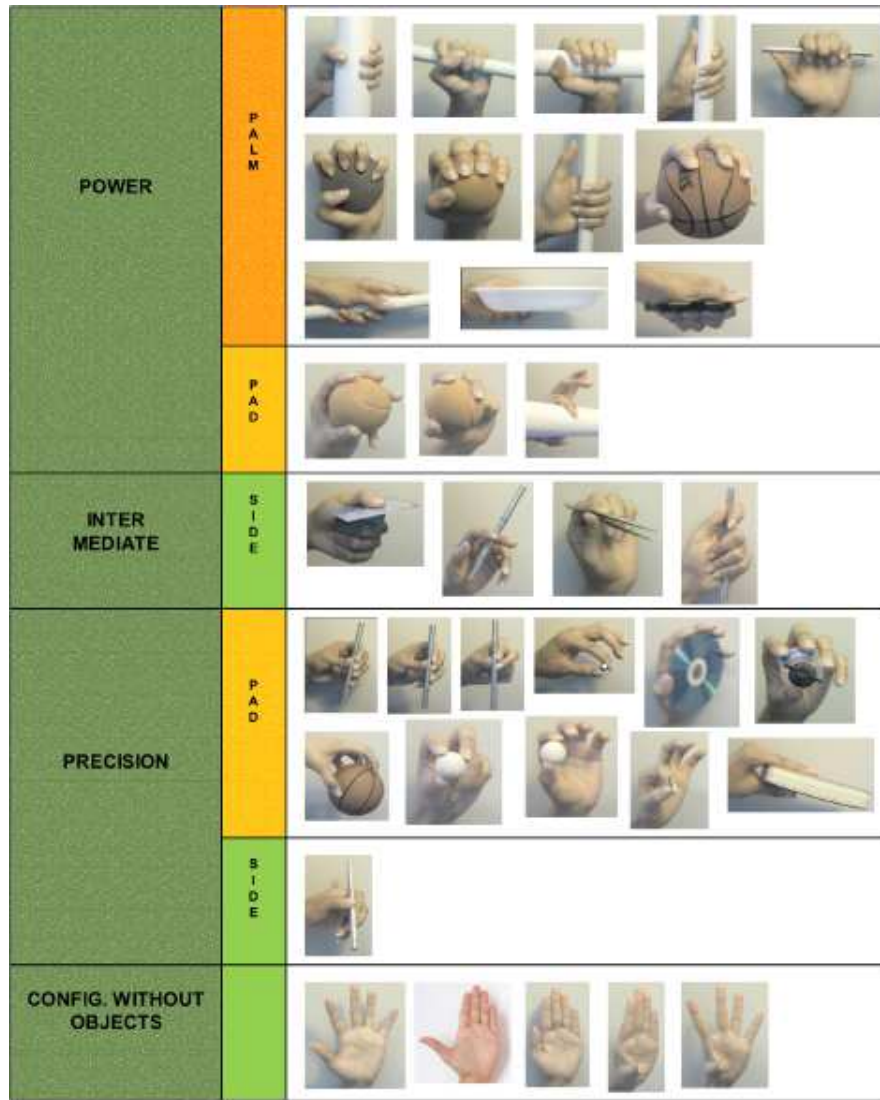


Fig. 20 Reference set of comprehensive human grasps and open-hand configurations used for PCA.

$$\hat{\mathbf{E}} = [\mathbf{e}_1 \ \mathbf{e}_2 \ \mathbf{e}_3] \quad (54)$$

composed of the three principal components of \mathbf{E} as a base of the robotic hand configuration space, thus allowing the control of the robotic hand motion in a configuration space of highly reduced dimensions with respect to the DOFs of the hand itself. Each hand grasp posture \mathbf{c}_i can be obtained by a suitable selection of the weights $[\alpha_1 \ \alpha_2 \ \alpha_3]^T \in \mathbb{R}^3$ of the postural synergies. Therefore, the projection $\hat{\mathbf{c}}_i$ of each

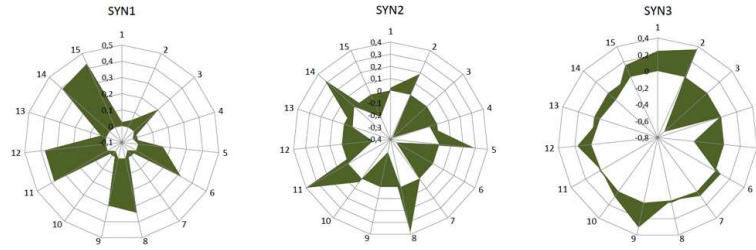


Fig. 21 In this figure, the angular change in degrees for each joint due to a positive unitary variation in α_1 , α_2 , and α_3 for the first three synergies is represented. The adduction/abduction, proximal and medial flexion joints are indicated from 1 to 3 for the thumb, from 4 to 6 for the index finger, from 7 to 9 for the middle finger, from 10 to 12 for the ring finger and finally from 13 to 15 for the little finger.

robotic hand configuration \mathbf{c}_i on the postural synergies subspace can be evaluated as

$$\hat{\mathbf{c}}_i = \bar{\mathbf{c}} + \hat{\mathbf{E}} \begin{bmatrix} \alpha_{1,i} \\ \alpha_{2,i} \\ \alpha_{3,i} \end{bmatrix}. \quad (55)$$

In the following, the three fundamental synergies derived for the DEXMART Hand, i.e. the robotic hand motions spanned by \mathbf{e}_1 , \mathbf{e}_2 and \mathbf{e}_3 respectively, are briefly described, referring to the minimum and maximum configuration of each synergy as the hand configurations obtained by means of, respectively, the minimum and maximum value of the corresponding synergy weights without violating the joint limits [21]. When the weights of the synergies are zero, the hand posture corresponds to the zero-offset position $\bar{\mathbf{c}}$. The vectors of the three synergies and the zero-offset vector of the DEXMART Hand are reported in Tab. 1.

The circular graphs represented in Fig. 21 are a useful tool for identifying the joints whose rotations are more involved in each synergy. From left to right, the angular variations in degrees for each joint due to a unitary variation of the corresponding synergy weight is represented for the first, the second and the third synergy. It is easy to observe how the adduction/abduction thumb joint motion (Joint 1) is more involved in the third synergy rather than in the first two. Moreover, in the third synergy the movement of the index and of the thumb are more engaged than for the other fingers. This justifies the use of the third synergy in order to grasp objects more precisely, especially for precision grasps and intermediate side grasps, where the position of the thumb and of the index is crucial, as the experiments reported in Sect. 3.4 demonstrate.

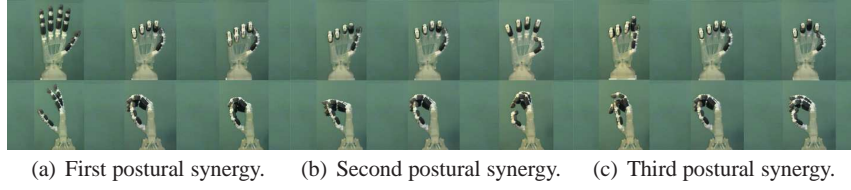


Fig. 22 Representation of the DEXMART Hand postural synergies. On the top of each figure, from left to right, a sequence of hand postures going from the minimum to the maximum configuration are represented. On the bottom the lateral views are reported.

3.3 Control With Postural Synergies

In order to perform the desired grasp, the value of the three eigenpostures weights $[\alpha_1 \ \alpha_2 \ \alpha_3]^T$ are computed by projection of the desired grasp posture in the synergies subspace:

$$\begin{bmatrix} \alpha_{1,i} \\ \alpha_{2,i} \\ \alpha_{3,i} \end{bmatrix} = \hat{\mathbf{E}}^\dagger (\mathbf{c}_i - \bar{\mathbf{c}}) \quad (56)$$

where $\hat{\mathbf{E}}^\dagger$ is the Moore-Penrose pseudo-inverse of the base matrix $\hat{\mathbf{E}}$. It is straightforward to note that the motions shown in Fig. 22(a), 22(b) and 22(c), derived by considering separately the three synergies, are obtained from (55) by assuming $\alpha_2 = 0$ and $\alpha_3 = 0$ for the first synergy, $\alpha_1 = 0$ and $\alpha_3 = 0$ for the second synergy and finally $\alpha_1 = 0$ and $\alpha_2 = 0$ for the third synergy.

The temporal value of the weights α_1 , α_2 , α_3 during grasp operations has to be chosen in such a way that, starting from the zero-offset position $\bar{\mathbf{c}}$ (i.e. $\alpha_1 = \alpha_2 = \alpha_3 = 0$), the hand opens during the reach in preparation for object grasp, and then closes reaching a suitable shape determined from (56) and depending on the original grasp configuration \mathbf{c}_i for the considered object. In the open-hand configuration, namely \mathbf{c}_0 , all the flexion joint angles are close to zero, and the corresponding values of α_1 , α_2 and α_3 can be determined from (56) by posing $\mathbf{c}_i = \mathbf{c}_0$.

The intermediate values of the synergy weights have been determined by assuming a suitable time interval for the grasp operation (six seconds for the whole reach to grasp phase, three seconds for both the opening and closing phases) and by linear interpolation of the α_1 , α_2 and α_3 values in the three reference configurations $\{\bar{\mathbf{c}}, \hat{\mathbf{c}}_0, \hat{\mathbf{c}}_i\}$.

Three synergies, shown in Figs. 22(a), 22(b) and 22(c) respectively, are now analyzed in detail. With reference to the first postural synergy (column \mathbf{e}_1 in Tab. 1), in the minimum configuration the proximal and medial flexion joint angles of all the fingers are all almost zero and increase their value during the motion toward the maximum configuration. The adduction/abduction movements are not very involved in this synergy. In Fig. 22(a) the minimum, zero-offset and maximum configuration in frontal and lateral view of the first postural synergy are represented. The second postural synergy (column \mathbf{e}_2 in Tab. 1) is characterized by a movement in opposite

Table 1 First three eigenpostures and zero offset vectors of the DEXMART Hand postural synergies subspace (data in degrees).

		e_1	e_2	e_3	$\bar{c}[deg]$
Thumb	adduction/abduction	0.0282	0.0235	-0.2454	-0.833
	proximal	0.0674	0.1874	-0.3639	20.5
	medial	0.2004	-0.3853	0.6991	34.7
Index	adduction/abduction	-0.0266	-0.0647	0.0228	2.92
	proximal	0.1575	0.2893	0.3648	34.9
	medial	0.3220	-0.3494	-0.0735	50.5
Middle	adduction/abduction	-0.0404	0.0069	-0.0675	-0.694
	proximal	0.3405	0.3794	0.0304	41.4
	medial	0.2999	-0.2948	-0.3034	42.2
Ring	adduction/abduction	-0.0374	0.0343	-0.0778	-1.11
	proximal	0.3775	0.3977	0.0200	45.5
	medial	0.3766	-0.2568	-0.1675	49.2
Little	adduction/abduction	0.0364	-0.0738	0.0720	0.694
	proximal	0.3892	0.3213	0.1273	48.7
	medial	0.4235	-0.2026	-0.1491	51.7

directions of the proximal and medial flexion joints. In this synergy, the adduction/abduction movements of all the fingers are more involved with respect to the first synergy for the index and the little finger. In Fig. 22(b) the minimum, zero-offset and maximum configurations of the second postural synergy are depicted in frontal and lateral views. In the third postural synergy (column e_3 in Tab. 1) the movement involves especially the index and the thumb. Thanks to this synergy, the movement of adduction/abduction of the thumb covers the whole joint range without violating other joint limits. This characteristic is crucial because the correct index/thumb position allows increasing the grasp accuracy, and thus achieving more stable grasps. This justifies the use of three predominant synergies for the hand control in order to improve the grasp performance. Finally, the excursion of the angles of adduction/abduction of the middle and ring fingers are quite involved in this synergy, more than in the first two. In Fig. 22(c) the minimum, zero-offset and maximum configuration in frontal and lateral views of the third postural synergy are represented.

3.4 Experimental Evaluation

The hand controller developed in the Matlab/Simulink environment is based on the RTAI-Linux realtime operating system. The Matlab Realtime Workshop toolbox has been used for the automatic generation of the real-time application of the DEXMART Hand controller. The user interface to the real-time application has been implemented by means of the Simulink External Mode capabilities, for which the RTAI-Linux support has been purposely developed.

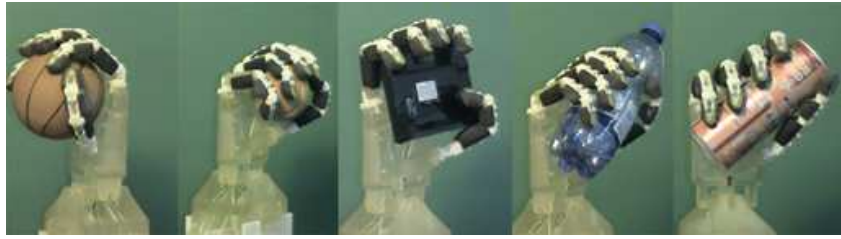


Fig. 23 Reproduced power grasps from the reference set of postures using the first three synergies.

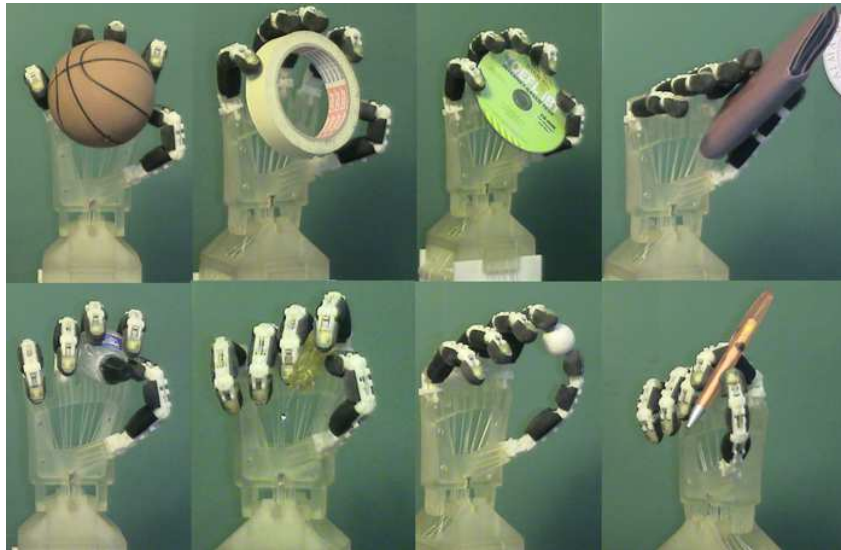


Fig. 24 Reproduced precision grasps from the reference set of postures using the first three synergies.

In the experiments, starting from the zero-offset position, the hand moves continuously in the synergies configuration subspace and goes in an open-hand configuration. Then, it closes reaching a configuration that depends on the particular grasp to be performed. During the closing phase, the weights of the three postural synergies are obtained by linear interpolation from those corresponding to the open-hand configuration to those suitable values unique for each object and computed using (56).

Experimental results reveal that, by using the three predominant eigengrasps, it is possible to reproduce several grasp configurations more precisely than in the case of using two synergies only [21].

The linear combination of the three synergies allows a power grasp of both cylinders and spheres of different dimensions by means of suitable opposition of the thumb, see Fig. 23.

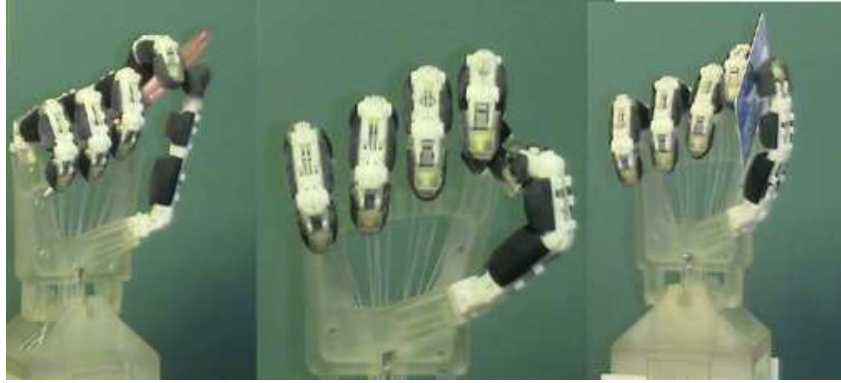


Fig. 25 Reproduced intermediate side grasps from the reference set of postures using the first three synergies.

In Fig. 24, the performance of precise grasp operations is reported considering different objects, achieving opposition of the thumb and index as well as precise grasps using from two to five fingers for prismatic and circular objects.

The reproduced intermediate side grasps from the reference set of postures is depicted in Fig. 25. All the evaluations of the experiments data have been carried out with the aid of the following tables. Table 2 reports the first three synergy weights computed by projection of the reference set of postures in the synergies subspace. In Tab. 3 the absolute value of the angle error of the adduction/abduction joint of the thumb obtained comparing the reference set of configurations and the reproduced configurations using two and three synergies are reported. Finally, the average of the joint errors in the case of using two and three synergies are reported in Tab. 4. The average of the joint errors is computed using the Euclidean norm

$$e = \frac{\|\mathbf{c}_i - \hat{\mathbf{c}}_i\|}{15}$$

By observing the first image from the left (pen, Configuration C27 in Tab. 2) of Fig. 25, it is interesting to note that this posture is very close to the minimum configuration of the third synergy; indeed the weight of the third synergy is high with respect to the other grasps, and thus the use of the third synergy is essential for this performance.

By looking at Tab. 3, it is possible to note that the use of the three predominant synergies reduces the error on the angular position of the adduction/abduction thumb joint for almost all the 36 configurations with respect to the case in which only two synergies are used.

In Tab. 3, the grasp configurations executed using only two synergies are marked with a star, while the new grasp configurations that have been performed successfully adding the third synergy are marked with a diamond. This table shows that, by introducing the third predominant synergy, the joint angle error of the thumb

is reduced for almost all the grasps configurations marked with a star, except for C10 (box), C16 (credit card) and C19 (pen). Nevertheless, a global improvement obtained using also the third synergy is evident observing the average joint angle errors reported in Tab. 4. Only for the configuration C14 no improvement has been obtained and this is confirmed by the very small value of the third synergy weight; this means that the third synergy gives almost no contribution to the variance of this posture. The improvement on the adduction/abduction thumb joint angle using the

Table 2 Synergy weights of the grasps from the reference set of postures.

Conf.	C1	C2*	C3	C4*	C5	C6	C7	C8
α_1	0.90	63.7	64.7	38.0	21.9	42.7	53.1	68.2
α_2	-3.47	28.1	-24.5	36.5	-33.6	-5.76	-8.21	-8.66
α_3	7.06	3.61	7.95	-21.2	-65.9	-2.33	-4.68	-8.56
Conf.	C9 \diamond	C10*	C11*	C12*	C13 \diamond	C14*	C15	C16*
α_1	-30.8	-4.00	58.8	12.3	-7.89	-18.9	8.86	63.7
α_2	-12.0	-117	9.39	-63.5	-59.0	8.47	1.36	39.3
α_3	21.4	-2.30	44.3	-14.0	27.6	0.15	-23.7	-8.38
Conf.	C17	C18	C19*	C20*	C21	C22	C23 \diamond	C24
α_1	13.7	42.7	67.4	-29.8	-18.4	-30.4	82.8	39.8
α_2	44.2	-43.2	28.4	122	-0.103	-30.2	2.58	23.3
α_3	-37.6	-13.2	16.0	25.3	17.7	11.2	31.7	18.3
Conf.	C25 \diamond	C26	C27 \diamond	C28	C29	C30	C31*	C32
α_1	35.4	65.3	75.9	81.8	-103	-120	26.3	-134
α_2	-17.8	1.82	19.8	26.4	-28.0	29.5	-0.933	4.10
α_3	27.6	18.8	-68.0	-20.3	27.8	18.7	31.0	-9.15
Conf.	C33	C34	C35	C36				
α_1	-134	-127	-134	-135				
α_2	4.20	18.3	4.96	3.73				
α_3	-10.2	-36.5	-5.04	-5.26				

third synergy is very clear at least for the configurations marked with a diamond. For what concerns Configuration C27 (pen, intermediate side grasp), the improvement can be seen mainly in the error average and it is spread on the thumb and index joints. These results show that the use of the third synergy allows grasping objects more precisely, especially when the position of the thumb and index is crucial, as in the case of precision grasps. The confirmation of this is given by the observation that the configurations marked with a diamond correspond to precision grasps, except for C27.

In Fig. 26, the distribution of the synergy weights adopted for executing the grasping experiments is shown in the space of the three predominant eigengrasps, and an example of a complete hand trajectory computed by linear interpolation of the synergies weights in the three reference configurations for the grasp of a generic object (a CD) is reported by the red dashed line. For the sake of clarity, only the weights of the grasps obtained during the experiments are reported, and only some of them are named. In this figure the full bullets represent the final configuration

Table 3 Adduction/abduction thumb joint angle error (in degrees) in the reproduced grasps from the reference set of postures obtained using two and three synergies.

Conf.	C1	C2*	C3	C4*	C5	C6	C7	C8
two syn	9.11	11.6	9.59	8.89	11.0	9.76	9.53	9.11
three syn	7.38	10.7	11.5	3.69	5.16	9.19	8.38	7.01
Conf.	C9 \circ	C10*	C11*	C12*	C13 \circ	C14*	C15	C16*
two syn	8.02	6.30	11.0	12.0	7.56	8.83	10.5	1.88
three syn	2.77	6.87	0.17	8.54	0.77	8.80	4.73	3.94
Conf.	C17	C18	C19*	C20*	C21	C22	C23 \circ	C24
two syn	9.41	9.35	8.26	11.2	8.65	7.60	11.6	10.8
three syn	0.186	12.6	12.2	4.97	4.30	4.84	3.79	6.33
Conf.	C25 \circ	C26	C27 \circ	C28	C29	C30	C31*	C32
two syn	9.74	8.95	8.23	7.91	5.59	6.48	9.89	14.5
three syn	2.98	13.6	8.46	2.93	1.22	1.88	2.28	12.3
Conf.	C33	C34	C35	C36				
two syn	14.5	14.0	5.50	5.45				
three syn	12.0	5.02	6.74	6.74				

Table 4 Average joint angle errors (in degrees) in the reproduced grasps from the reference set of postures obtained using two and three synergies.

Conf.	C1	C2*	C3	C4*	C5	C6	C7	C8
two syn	1.81	1.84	1.83	2.70	4.89	2.25	2.24	2.12
three syn	1.75	1.82	1.75	2.30	2.16	2.24	2.22	2.05
Conf.	C9 \circ	C10*	C11*	C12*	C13 \circ	C14*	C15	C16*
two syn	2.21	1.38	3.48	1.90	2.64	1.63	3.62	1.56
three syn	1.69	1.37	1.84	1.65	1.89	1.63	3.26	1.46
Conf.	C17	C18	C19*	C20*	C21	C22	C23 \circ	C24
two syn	4.11	2.01	3.20	2.19	2.06	3.78	2.77	2.34
three syn	3.26	1.81	3.02	1.40	1.68	3.70	1.79	1.99
Conf.	C25 \circ	C26	C27 \circ	C28	C29	C30	C31*	C32
two syn	2.95	2.31	4.83	4.27	3.29	4.05	2.60	2.00
three syn	2.31	1.94	1.66	4.05	2.72	3.86	1.57	1.90
Conf.	C33	C34	C35	C36				
two syn	1.92	4.99	1.99	1.70				
three syn	1.80	4.35	1.97	1.66				

weights corresponding to the grasps performed also in the previous work [21]. The triangles represent the final configuration weights corresponding to the objects that have been grasped thanks to the use of the third synergy also. Finally, the circles represent the final synergy weights corresponding to the synthesized grasps of different grasp/object pairs (Fig. 28(b)) not included in the table of Fig. 20 and obtained by projection in the synergies subspace of the desired configuration of the hand. This desired configuration is obtained experimentally, moving singularly the joints in order to realize the desired grasp.

In Fig. 27 two grasp configurations executed using both two and three synergies are represented. From left to right the first pictures of the ball and of the CD are the

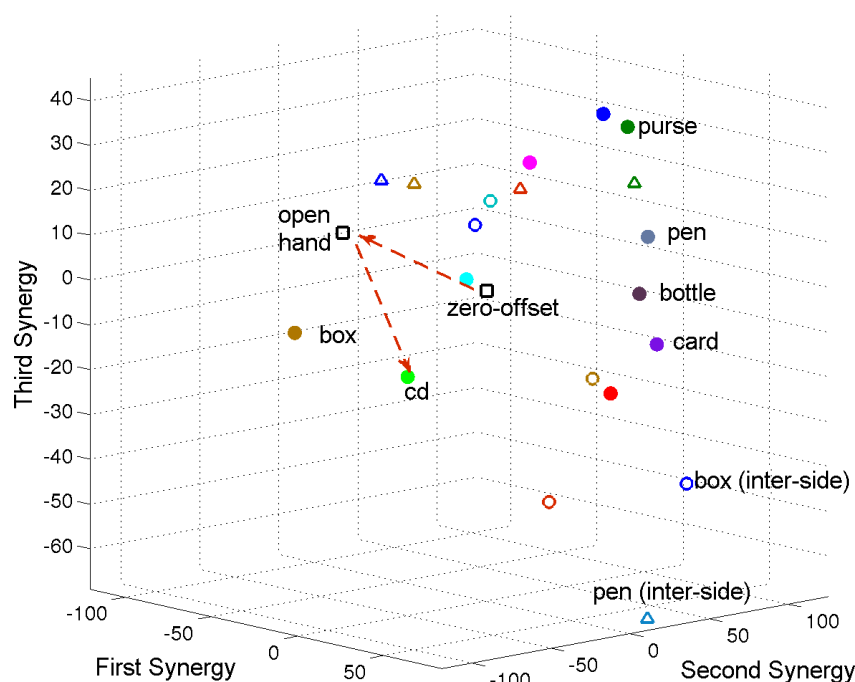


Fig. 26 The distribution of hand postures in the space of the first three postural synergies is represented, distinguishing between the object graspable also using the first two synergies only (full bullets), the objects graspable thanks to the use of the third synergy (triangles), and the synthesized grasps obtained by projection (circles).

ones executed using three synergies. From these pictures, the improvement on the position of the thumb can be noticed thanks to the introduction of the third synergy in the hand control.

The grasps realized above show that through the use of three synergies we can reproduce the matrix of the reference set of postures (Fig. 20) with accuracy greater than 85%.

The idea now is to extend the method in order to grasp any object not necessarily contained in the reference table. The advantage of the synergies subspace is that of simplifying grasp synthesis of common objects using also complex hand shapes typical of human manipulation.

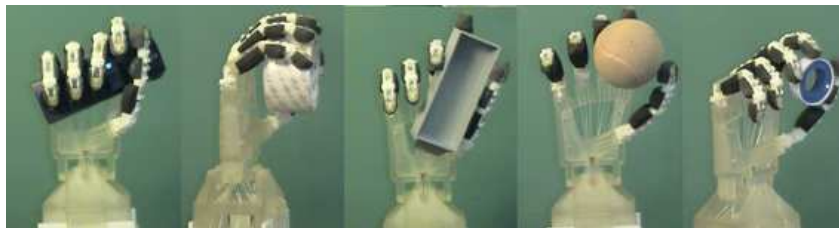
To accomplish this goal, we have selected grasps of five common objects in Fig. 28(a). The object/grasp pairs have been chosen so as to cover the entire variety in recently proposed taxonomy [20], namely a power palm grasp, a power pad grasp, an intermediate side grasp, a precision pad grasp, and a precision side grasp. Moreover, the choices have been made with the intent to imitate the typical modality of human manipulation. The selected grasp configurations are unusual for a typical application of robotic manipulation as they are carried out by a robotic hand with high dexterity and anthropomorphism. In fact, they constitute a high standard



Fig. 27 Comparison between two grasps configuration executed using both two and three synergies. From left to right the first pictures of the ball and of the CD are the ones executed using three synergies.

POWER		INTERMEDIATE	PRECISION	
PALM	PAD	SIDE	PAD	SIDE
				

(a) Reference set of human grasps.



(b) Synthesized grasps with the DEXMART Hand.

Fig. 28 On the top the reference set of human grasps, not included in the PCA analysis, covering the entire variety of grasps in recently proposed taxonomies, is depicted. On the bottom the synthesized grasps realized with the DEXMART Hand using synergies subspace projection is shown. A power palm grasp, a power pad grasp, an intermediate side grasp, a precision pad grasp and a precision side grasp are reported from left to right.

for robotic hands currently on the market and designed for applications of service robotics and prosthetics. On the other hand, the synthesis of this kind of grasps involves complex problems of planning and control. The high number of DOFs and complex kinematics similar to that of the human hand is essential for this specific type of tasks. Despite this, the DOFs have to be managed.

Through a teaching-by-showing technique, the use of synergies allows reducing significantly synthesis complexity. By singularly guiding the finger joints, the hand

has been carried to the desired grasp configuration and the joint displacement vector has been recorded. Through the projection of the desired configuration in the synergies subspace we have derived their weights in the final configuration \hat{c}_i . The weights are subsequently used in the control algorithm that performs motion during reach to grasp and realize the desired final grasp configuration, see Fig. 28(b).

Table 5 Synergy weights of the grasps in Fig. 28(b) (from left to right).

Conf.	G1	G2	G3	G4	G5
α_1	84.3	-6.61	16.7	-14.4	42.8
α_2	34.8	8.96	20.6	7.93	18.5
α_3	-37.3	18.6	-47.1	12.9	-16.2

The weights shown in Tab. 5 indicate the contribution rate of each synergy to achieve the final configuration. Referring to what we have previously argued about the use of the third synergy, for the grasp represented in the third image of Fig. 28(b) (G3), the weight of the third synergy greatly influences the success of the grasp, see Tab. 5.

The experimental results demonstrate a good choice of the reference set of postures to retrieve the synergies subspace, and confirm that the planning/control method based on synergies can work efficiently for every object and grasp choice throughout a complete taxonomy. During reach to grasp, the hand behaves like a human hand reaching impressive human like shape using a small effort in planning.

4 Conclusion

In this chapter, some issues related to the control of anthropomorphic sensorised hands have been addressed. First, the problem of computing online the optimal contact forces to grasp an object has been considered, assuming that these forces may vary during task execution, thanks to the availability of force/torque sensors at the fingertips of the DEXMART Hand. The proposed algorithm takes into account the maximum joint torques that can be provided by the fingers and has been extended to bimanual manipulation tasks with a limited increase of the computational complexity, thanks to a novel load sharing technique. The other interesting feature of anthropomorphic manipulation, especially in the bimanual case, is the availability of redundant degrees of freedom. These have been suitably exploited to design a multi-priority control approach that allows satisfying a certain number of secondary tasks, aimed at ensuring grasp stability and manipulation dexterity, besides the main task corresponding to the desired object motion. Finally, anthropomorphism has been exploited for the development of a human-like grasping approach based on the synergic motions that can be observed in the human hand. In detail, the synthesis and control of grasping for the DEXMART Hand have been simplified by computing a reduced configuration subspace based on few predominant postural synergies.

This approach has been evaluated at kinematic level, showing that both power and precise grasps can be performed using up to the third predominant synergy.

Acknowledgements

The research leading to these results has been supported by the DEXMART Large-scale integrating project, which has received funding from the European Community's Seventh Framework Programme (FP7/2007-2013) under grant agreement ICT-216239. The authors are solely responsible for its content. It does not represent the opinion of the European Community and the Community is not responsible for any use that might be made of the information contained therein.

The authors would like to thank Fabrizio Caccavale, Giuseppe Muscio and Francesco Pierri for their contribution in the design and implementation of the control approach with redundancy resolution.

References

1. G. Antonelli, "Stability analysis for prioritized closed-loop inverse kinematic algorithms for redundant robotic systems", *IEEE Transactions on Robotics*, vol. 25 pp. 985–994, 2009.
2. G. Berselli, G. Borghesan, M. Brandi, C. Melchiorri, C. Natale, G. Palli, S. Pirozzi, G. Vassura, "Integrated mechatronic design for a new generation of robotic hands", *IFAC Symposium on Robot Control*, Gifu, 2009.
3. G. Berselli, M. Piccinini, G. Palli, G. Vassura, "Engineering design of fluid-filled soft covers for robotic contact interfaces: Guidelines, nonlinear modelling, and experimental validation", *IEEE Transactions on Robotics*, vol. 27, pp. 436–449, 2011.
4. G. Berselli, M. Piccinini, G. Vassura, "On designing structured soft covers for robotic limbs with predetermined compliance", *ASME International Design Engineering Technical Conferences*, Montréal, 2010.
5. G. Berselli, G. Vassura, "Differentiated layer design to modify the compliance of soft pads for robotic limbs", *IEEE International Conference on Robotics and Automation*, Kobe, 2009.
6. L. Biagiotti, F. Lotti, C. Melchiorri, G. Palli, P. Tiezzi, G. Vassura, "Development of UB Hand 3: Early results", *IEEE International Conference on Robotics and Automation*, Barcelona, 2005.
7. A. Bicchi, M. Gabiccini, M. Santello, "Modelling natural and artificial hands with synergies", *Philosophical Transactions of the Royal Society B: Biological Sciences*, vol. 366, pp. 3153–3161, 2011.
8. A. Bicchi, D. Prattichizzo, "Manipulability of cooperative robots with unactuated joints and closed-chain mechanisms", *IEEE Transactions on Robotics and Automation*, vol. 16, pp. 336–345, 2000.
9. G. Borghesan, G. Palli, C. Melchiorri, "Design of tendon-driven robotic fingers: Modelling and control issues", *IEEE International Conference on Robotics and Automation*, Anchorage, AK, 2010.
10. C. Brown, H. Asada, "Inter-finger coordination and postural synergies in robot hands via mechanical implementation of principal components analysis", *IEEE/RSJ International Conference on Intelligent Robots and Systems*, San Diego, CA, 2007.
11. M. Buss, H. Hashimoto and J. B. Moore, "Dextrous hand grasping force optimization", *IEEE Transactions on Robotics and Automation*, vol. 12, pp. 406–418, 1996.

12. M. Buss, L. Faybusovich and J. B. Moore, "Dikin-type algorithms for dextrous grasping force optimization", *International Journal of Robotics Research*, vol. 17, pp. 831–839, 1998.
13. M. Ciocarlie, P. Allen, "Hand posture subspaces for dexterous robotic grasping", *International Journal of Robotics Research*, vol. 28, pp. 851–867, 2009.
14. M. Ciocarlie, P. Allen, "On-line interactive dextrous grasping", *6th International Conference on Haptics: Perception, Devices and Scenarios*, Madrid, 2008.
15. M. Ciocarlie, C. Goldfeder, P. Allen, "Dimensionality reduction for hand-independent dexterous robotic grasping", *IEEE/RSJ International Conference on Intelligent Robots and Systems*, San Diego, 2007.
16. J. Coelho, R. Grupen, "A control basis for learning multifingered grasps" *Journal of Robotic Systems*, vol. 14, pp. 545–557, 1997.
17. M. Cutkosky, "On grasp choice, grasp models, and the design of hands for manufacturing tasks", *IEEE Transactions on Robotics and Automation*, vol. 5, pp. 269–279, 1989.
18. DEXMART Project website, <http://www.dexmart.eu/>.
19. L. Faybusovich, "Dikin's algorithm for matrix linear programming problems", in *System Modelling and Optimization*, J. Henry, J.-P. Yvon (Eds.), pp. 237–247, Springer, New York, 1994.
20. T. Feix, R. Pawlik, H. Schmiedmayer, J. Romero, D. Kragic, "The generation of a comprehensive grasp taxonomy", *Robotics: Science and Systems, Workshop on "Understanding the Human Hand for Advancing Robotic Manipulation"*, Seattle, WA, 2009.
21. F. Ficuciello, G. Palli, C. Melchiorri, B. Siciliano, "Experimental evaluation of postural synergies during reach to grasp with the UB Hand IV", *IEEE/RSJ International Conference on Intelligent Robots and Systems*, San Francisco, CA, 2011.
22. M. Gabiccini, A. Bicchi, "On the role of hand synergies in the optimal choice of grasping forces", *Robotics: Science and Systems*, Zaragoza, 2010.
23. T. Geng, M. Lee, M. Hulse, "Transferring human grasping synergies to a robot", *Mechatronics*, vol. 21, pp. 272–284, 2011.
24. G. Gioioso, G. Salvietti, M. Malvezzi, D. Prattichizzo, "Mapping synergies from human to robotic hands with dissimilar kinematics: An object based approach", *IEEE International Conference on Robotics and Automation, Workshop on Manipulation Under Uncertainty*, Shanghai, 2011.
25. L. Han, J.C. Trinkle, "The instantaneous kinematics of manipulation", *IEEE International Conference on Robotics and Automation*, Leuven, 1998.
26. L. Han, J.C. Trinkle, Z.X. Li, "Grasp analysis as linear matrix inequality problems", *IEEE Transactions on Robotics and Automation*, vol. 16, pp. 663–674, 2000.
27. U. Helmke, K. Hper, J.B. Moore, "Quadratically convergent algorithms for optimal dextrous hand grasping", *em IEEE Transactions on Robotics and Automation*, vol. 18, pp. 138–146, 2002.
28. U. Helmke, J. B. Moore, *Optimization and Dynamic Systems*, Springer-Verlag, New York, 1993.
29. T. Iberall, "Human prehension and dextrous robot hands", *International Journal of Robotics Research*, vol. 16, pp. 285–299, 1997.
30. Z.X. Li, Z. Quin, S. Jiang, L. Han, "Coordinated motion generation and real-time grasping force control for multifingered manipulation", *IEEE International Conference on Robotics and Automation*, Leuven, 1998.
31. V. Lippiello, F. Ruggiero, L. Villani, "Exploiting redundancy in closed-loop inverse kinematics for dextrous object manipulation", *International Conference on Advanced Robotics*, Munich, 2009.
32. V. Lippiello, B. Siciliano, L. Villani, "Online dextrous-hand grasping force optimization with dynamic torque constraints selection", *IEEE International Conference on Robotics and Automation*, Shanghai, 2011.
33. V. Lippiello, B. Siciliano, L. Villani, "A grasping force optimization algorithm with dynamic torque constraints selection for multi-fingered robotic hands", *American Control Conference*, San Francisco, CA, 2011.
34. G. Liu, J. Xu, Z. Li, "On geometric algorithms for real-time grasping force optimization", *IEEE Transactions on Control System Technology*, vol. 12, pp. 843–859, 2004.

35. F. Lotti, G. Vassura, "A novel approach to mechanical design of articulated fingers for robotic hands", *IEEE/RSJ International Conference on Intelligent Robots and Systems*, Lausanne, 2002.
36. N. Mansard, F. Chaumette, "Task sequencing for high-level sensor-based control", *IEEE Transactions on Robotics and Automation*, vol. 23, pp. 60–72, 2007.
37. C. Mason, J. Gomez, T. Ebner, "Hand synergies during reach-to-grasp", *Journal of Neurophysiology*, vol. 86, pp. 2896–2910, 2001.
38. G. Matrone, C. Cipriani, E. Secco, G. Magenes, M. Carrozza, "Principal components analysis based control of a multi-dof underactuated prosthetic hand", *Journal of NeuroEngineering and Rehabilitation*, vol. 7, no. 16, pp. 1–16, 2010.
39. D. Montana, "The kinematics of contact and grasp", *International Journal of Robotics Research*, vol. 7, no. 3, pp. 17–32, 1988.
40. D. Montana, "The kinematics of multi-fingered manipulation", *IEEE Transactions on Robotics and Automation*, vol. 11, pp. 491–503, 1995.
41. R. Murray, Z.X. Li, S. Sastry, *A Mathematical Introduction to Robotic Manipulation*, CRC Press, Boca Raton, FL, 1994.
42. J. Napier, "The prehensile movements of the human hand", *Journal of Bone and Joint Surgery*, vol. 38-B, pp. 902–913, 1956.
43. A.M. Okamura, N. Smaby, M.R. Cutkosky, "An overview of dextrous manipulation", *IEEE International Conference on Robotics and Automation*, San Francisco, CA, 2000.
44. G. Palli, G. Borghesan, C. Melchiorri, "Modelling, identification and control of tendon-based actuation systems", *IEEE Transactions on Robotics*, vol. 27, pp. 1–14, 2011.
45. R. Platt, A.H. Fagg, R. Grupen, "Null-space grasp control: Theory and experiments", *IEEE Transactions on Robotics*, vol. 26, pp. 282–295, 2010.
46. J. Ponce, S. Sullivan, A. Sudsang, J. Boissonnat, J. Merlet, "On computing four-finger equilibrium and force-closure grasps of polyhedral objects", *International Journal of Robotic Research*, vol. 16, pp. 11–35, 1996.
47. D. Prattichizzo, M. Malvezzi, A. Bicchi, "On motion and force controllability of grasping hands with postural synergies", *Robotics: Science and Systems*, Zaragoza, 2010.
48. D. Prattichizzo, M. Malvezzi, M. Gabiccini, A. Bicchi, "On the manipulability ellipsoids of underactuated robotic hands with compliance", *Robotics and Autonomous Systems*, vol. 60, pp. 337–346, 2012.
49. D. Prattichizzo, J.C. Trinkle, "Grasping", in *Springer Handbook of Robotics*, B. Siciliano, O. Khatib (Eds.), pp. 671–700, Springer, Heidelberg, 2008.
50. C. Remond, V. Perdereau, M. Drouin, "A multi-fingered hand control structure with on-line grasping force optimization", *IEEE/ASME International Conference on Advanced Intelligent Mechatronics*, Como, 2001.
51. J. Romero, T. Feix, H. Kjellstrom, D. Kragic, "Spatio-temporal modelling of grasping actions", *IEEE/RSJ International Conference on Intelligent Robots and Systems*, Taipei, 2010.
52. M. Santello, M. Flanders, J. Soechting, "Postural hand synergies for tool use", *Journal of Neuroscience*, vol. 18, pp. 10105–10115, 1998.
53. J.P. Saut, C. Remond, V. Perdereau, M. Drouin, "Online computation of grasping force in multi-fingered hands", *IEEE/RSJ International Conference on Intelligent Robots and Systems*, Edmonton, 2005.
54. T. Shlegl, M. Buss, T. Omata, G. Schmidt, "Fast dextrous regrasping with optimal contact force and contact sensor-based impedance control", *IEEE International Conference on Robotics and Automation*, Seoul, 2001.
55. B. Siciliano, L. Sciavicco, L. Villani, G. Oriolo, *Robotics: Modelling, Planning and Control*, Springer, London, 2009.
56. M. Uchiyama, "A unified approach to load sharing, motion decomposing, and force sensing of dual arm robots", in *Robotics Research: The Fifth International Symposium*, H. Miura, S. Arimoto (Eds.), pp. 225–232, MIT Press, Cambridge, MA, 1994.
57. J. Vilaplana, J. Coronado, "A neural network model for coordination of hand gesture during reach to grasp", *Neural Networks*, vol. 19, pp. 12–30, 2006.

58. I.D. Walker, S.I. Marcus, R.A. Freeman, "Distribution of dynamic loads for multiple cooperating robot manipulators", *Journal of Robotic Systems*, vol. 9, pp. 35–47, 1989.
59. T. Wimboeck, B. Jan, G. Hirzinger, "Synergy-level impedance control for a multifingered hand", *IEEE/RSJ International Conference on Intelligent Robots and Systems*, San Francisco, CA, 2011.
60. J. Xu, Y. Lou, Z. Li, "Grasping force optimization for whole hand grasping", *IEEE/RSJ International Conference on Intelligent Robots and Systems*, Beijing, 2006.
61. Y.F. Zheng, J.Y.S. Luh, "Optimal load distribution for two industrial robots handling a single object", *IEEE International Conference on Robotics and Automation*, Philadelphia, PA, 1988.